

Broadband generation of perfect Poincaré beams via dielectric spin-multiplexed metasurface

Mingze Liu^{1,2}, Pengcheng Huo^{1,2}, Wenqi Zhu^{3,4}, Cheng Zhang⁵, Si Zhang¹, Maowen Song¹, Song Zhang¹, Qianwei Zhou¹, Lu Chen^{3,4}, Henri J. Lezec³, Amit Agrawal^{3,4}, Yanqing Lu^{1,2} and Ting Xu^{1,2}

1. National Laboratory of Solid-State Microstructures, Jiangsu Key Laboratory of Artificial Functional Materials, College of Engineering and Applied Sciences, Nanjing University, Nanjing 210093, China
2. Collaborative Innovation Center of Advanced Microstructures, Nanjing 210093, China
3. Physical Measurement Laboratory, National Institute of Standards and Technology, Gaithersburg, Maryland 20899, United States
4. Maryland NanoCenter, University of Maryland, College Park, Maryland 20899, United States
5. School of Optical and Electronic Information, Wuhan National Laboratory for Optoelectronics, Huazhong University of Science and Technology, Wuhan 430074, China.

Abstract

The term Poincaré beam, which describes the space-variant polarization of a light beam carrying spin angular momentum (SAM) and orbital angular momentum (OAM), plays an important role in various optical applications. Since the radius of a Poincaré beam conventionally depends on the topological charge number, it is difficult to generate a stable and high-quality Poincaré beam by two optical vortices with different topological charge numbers, as the Poincaré beam formed in this way collapses upon propagation. Here, based on an all-dielectric metasurface platform, we experimentally demonstrate broadband generation of a generalized perfect Poincaré beam (PPB), whose radius is independent of the topological charge number. By utilizing a phase-only modulation approach, a single-layer spin-multiplexed metasurface composed of an array of subwavelength-spaced titanium dioxide nanopillars is shown to achieve all the states of PPBs on the hybrid-order Poincaré Sphere for visible light. Furthermore, as a proof-of-concept demonstration, a metasurface encoding multidimensional SAM and OAM states in the parallel channels of elliptical and circular PPBs is implemented for optical information encryption. We envision that this work will provide a compact and efficient platform for generation of PPBs for visible light, and may promote their applications in optical communications, information encryption, optical data storage and quantum information sciences.

1. Introduction

Polarization and phase are two intrinsic properties of light¹. Light can possess a spin angular momentum (SAM) of $\sigma\hbar$ ($\sigma = \pm 1$) per photon depending on the chirality of circular polarization², and an orbital angular momentum (OAM) of $l\hbar$ (where l is the topological charge number) per photon depending on its helical phase structure³. SAM and OAM constitute the total angular momentum ($J = \sigma\hbar + l\hbar$) of a light beam⁴. The hybrid-order Poincaré Sphere (HyOPS)⁵, which generalizes Poincaré Sphere (PS)⁶ and higher-order Poincaré Sphere (HOPS)⁷, has been developed to describe the total angular momentum and the evolution of polarization and phase of light. The poles of the HyOPS denote two orthogonal, circularly polarized states of optical vortices⁸ with arbitrary topological charge numbers. Each point on the HyOPS describes the space-variant polarization field of a light beam carrying OAM, which can be represented by a linear superposition of the two poles and is generally referred to as Poincaré beam⁹. In particular, the optical vortices and cylindrical vector vortex beams¹⁰ described by the poles and equator of the HyOPS, respectively, have been demonstrated and applied in a number of applications¹¹, such as optical trapping, high-resolution microscopy, optical communication, nonlinear optics and optical encryption¹². However, the beam radii of these conventional Poincaré beams always depends on their topological charge number, hindering their applications in some cases, for *e.g.*, coupling of multiple Poincaré beams into a single optical fiber for mode division multiplexing¹³. In addition, it is difficult to generate a stable and high-quality Poincaré beam by two orthogonally circularly polarized optical vortices with very different topological charge numbers, as the Poincaré beam formed in this way would easily collapse upon propagation¹⁴.

Recently, the concept of perfect optical vortices (POVs) has been proposed to overcome the above limitations because their ring radii are independent of the topologic charges¹⁵. Consequently, perfect Poincaré beams (PPBs), as the linear superposition of POVs, have been demonstrated using selective combinations of conventional optical components, such as axicons, spatial light modulators, q -plates and Fourier transform lenses¹⁶⁻¹⁸. However, the complex light path and bulky footprint of optical components generally required in these approaches make them non-ideal for integration into compact nanophotonic platforms. Furthermore, optical aberrations caused by misalignment between the different optical components can easily deteriorate the quality of PPBs. In addition, conventional spatial light modulators and q -plates have micron-scale sampling pixel sizes that significantly limits the spatial density of the generated PPBs array.

Metasurfaces, made up of nanoscale optical scatters, can arbitrarily modulate the phase, polarization, and amplitude of light with deep subwavelength spatial resolution, and thus provides an efficient, versatile and integration-friendly platform for compact planar optics¹⁹⁻³⁰. In particular, due to the flexible design freedom offered by them, transmissive metasurfaces

have been applied to a wide variety of functional planar optics, such as imaging lenses³¹⁻³⁵, metaholograms³⁶⁻³⁸, nonlinear optics^{39,40}, and structured beam generators⁴¹⁻⁴³. Recently, a plasmonic metasurface was shown to generate POVs⁴⁴; however, it suffers from low efficiency due to the large ohmic absorption caused by the constituent metallic nanostructures. A silicon metasurface has also been designed to generate PPBs⁴⁵; however, this design requires simultaneous phase and amplitude modulation and a complicated oblique incidence scheme, which further limit its efficiency and operating bandwidth.

In this work, based on an all-dielectric metasurface, we propose and experimentally demonstrate a compact platform for broadband generation of generalized PPBs, including both elliptical and circular shapes. Through phase-only modulation, a single-layer metasurface composed of subwavelength-spaced titanium dioxide (TiO₂) nanopillars can straightforwardly achieve all the states of PPBs on the HyOPS for visible light, without the requirement of any additional optical elements. By combining both geometric phase and propagation phase modulation⁴⁶, the designed spin-multiplexed metasurface can provide two arbitrary, fully uncorrelated phase profiles for the two orthogonal circular polarizations of incident light. By changing the polarization states of incident light, all orders of PPBs with arbitrary phase and polarization distributions can be generated. Furthermore, as a proof-of-concept demonstration, a metasurface encoding multidimensional SAM and OAM states in parallel channels for elliptical and circular PPBs is implemented for optical information encryption. We envision that this work will provide a platform for efficient generation of PPBs for visible light and may promote their applications in optical communications, information encryption, optical data storage and quantum information science. Furthermore, this method to achieve complete and independent phase control of orthogonal circular polarization states at the single pixel level also can be used to design vectorial metasurface to generate arbitrary 3D vectorial field distribution for 3D vectorial holography application⁴⁷. This vectorial metasurface may promote the development of compact and highly-integrated optical system for polarization holography, Stokes holography, holographic trap display, multidimensional data storage and optical microscopic imaging.

2. Results

Design of metasurface to generate generalized PPBs

The vectorial field of a monochromatic paraxial light beam can be represented by the superposition of scalar fields with orthogonal polarization states¹¹. Considering the orthogonal circular polarization basis and two POVs with same ring radius but different topological charges, a PPB can be described as:

$$|U_N\rangle = \cos\left(\frac{\alpha}{2}\right)e^{i\beta/2}|\text{POV}_R, l_m\rangle + \sin\left(\frac{\alpha}{2}\right)e^{-i\beta/2}|\text{POV}_L, l_n\rangle \quad (1)$$

where $|\text{POV}_R, l_m\rangle$ and $|\text{POV}_L, l_n\rangle$ denote the right-handed circularly polarized (RCP) and left-handed circularly polarized (LCP) POV with same ellipticity, and different topological charge numbers of l_m and l_n , respectively. $\cos(\frac{\alpha}{2})$ and $\sin(\frac{\alpha}{2})$ represent the amplitude of RCP and LCP POV and β is the relatively phase difference between them, where $\alpha \in [0, \pi]$ and $\beta \in [0, 2\pi]$. $|U_N\rangle$ is an arbitrary point on the surface of HyOPS with spherical coordinates (α, β) . Figure 1a shows examples of various elliptical PPBs and their mapping points on the HyOPS. Each point on the surface of the HyOPS denotes a state of a PPB with space-variant polarization and phase distribution. The polarization distribution of each state can be determined by polarization order $p = (l_m - l_n)/2$ and the HyOPS spherical coordinates (α, β) . The phase distribution of the PPB is characterized by the topological Pancharatnam charge $l_p = (l_m + l_n)/2$ ^{14,45}. Two poles of the HyOPS are represented by two elliptical POVs with same ellipticity factor $\gamma = 1.2$ and uniform circular polarization (depicted by red arrows) but different topological charge numbers $l_m = 5$ and $l_n = 10$. The annular intensity profiles at other points on the HyOPS are also of the same ring radius; and due to their anisotropic linear polarization distributions (depicted by red arrows), these elliptical hollow beams can be transformed to exhibit distinct intensity patterns by using a vertical linear polarizer (indicated by the white double arrow).

In principle, a POV can be generated by taking the Fourier transform of a higher-order Bessel beam¹⁵. Due to the difficulty of experimentally generating an ideal Bessel beam, here we consider the Fourier transform of a higher-order Bessel-Gaussian beam instead. To be specific, a Gaussian beam can be transformed into a POV by passing it through a spiral phase plate, an axicon, and a Fourier transform lens. In terms of the Fourier transform theory, the complex field amplitude of the POV with uniform polarization in the rear focal plane of a lens can be obtained as (see Supplementary Note 1 for details):

$$\vec{E}(r, \varphi) = \frac{\omega_g i^{l-1}}{\omega_\gamma} \exp(il\varphi) \exp\left(\frac{-(r-R_\gamma)^2}{\omega_\gamma^2}\right) \begin{bmatrix} 1 \\ \pm i \end{bmatrix} \quad (2)$$

where (r, φ) are the polar coordinates, ω_g is the waist of the input Gaussian beam, ω_γ is the waist of the Gaussian beam in the rear focal plane, and l is the topological charge. $R_\gamma = \gamma k_r f/k$, where k_r is the radial wavevector relying on the numerical aperture (NA) of the axicon, $k = 2\pi/\lambda_0$ is the free-space wavevector, and f is the focal length of lens. It is obvious that the amplitude of the POV is shaped by a Gaussian function, which has a maximum value at $r = R_\gamma$. The radii of the POV along the vertical and horizontal directions can be expressed as $R_\perp = f\text{NA}$ and $R_\parallel = \gamma f\text{NA}$, respectively, which are independent of

topological charges. Therefore, depending on the values of three parameters (γ, f, NA), the intensity profile and radius along the major and minor axis of POV can be arbitrarily controlled. Therefore, customized shaping of the POV guarantees the generation of arbitrary annular intensity distribution of the PPB, providing sufficient variables for potential use in optical information encryption.

Due to the unique capability of flexible manipulation of the properties of light, a metasurface is able to integrate multiple functions of different optical elements, such as the spiral phase plate, axicon and Fourier transform lens as mentioned above, into a single monolithic device for PPB generation. For a polarized light beam normally incident onto the metasurface, it can be decomposed into LCP and RCP spin eigenstates corresponding to 2D Jones vectors: $|\text{LCP}\rangle = \begin{bmatrix} 1 \\ i \end{bmatrix}$ and $|\text{RCP}\rangle = \begin{bmatrix} 1 \\ -i \end{bmatrix}$. In order to generate two completely different POVs, the spin-multiplexed metasurface is required to provide two independent spatial phase profiles $\varphi_1(x, y)$ and $\varphi_2(x, y)$ respectively corresponding to $|\text{LCP}\rangle$ and $|\text{RCP}\rangle$ state (see Supplementary Note 2 for details). That is, for LCP incident light, the metasurface implements the transformation: $|\text{LCP}\rangle \rightarrow |\text{POV}_R, l_m\rangle$ (Figure. 1b). The output beam $|\text{POV}_R, l_m\rangle$ has flipped handedness compared to the incident light. Similarly, for the RCP incident light, the metasurface transforms it to a different POV with LCP state and topological charge of l_n : $|\text{RCP}\rangle \rightarrow |\text{POV}_L, l_n\rangle$ (Figure. 1c). Therefore, the metasurface can be described by a Jones matrix $J(x, y)$ which simultaneously satisfies $J(x, y)|\text{LCP}\rangle = \exp[i\varphi_1(x, y)]|\text{RCP}\rangle$ and $J(x, y)|\text{RCP}\rangle = \exp[i\varphi_2(x, y)]|\text{LCP}\rangle$. The required Jones matrix takes the form:

$$J(x, y) = \begin{bmatrix} \frac{\exp[i\varphi_1(x, y)] + \exp[i\varphi_2(x, y)]}{2} & \frac{i\exp[i\varphi_2(x, y)] - i\exp[i\varphi_1(x, y)]}{2} \\ \frac{i\exp[i\varphi_2(x, y)] - i\exp[i\varphi_1(x, y)]}{2} & \frac{-\exp[i\varphi_1(x, y)] - \exp[i\varphi_2(x, y)]}{2} \end{bmatrix} \quad (3)$$

Due to the symmetric and unitary conditions, $J(x, y)$ can be written in a standard form $J(x, y) = R\Lambda R^{-1}$, where R is a real unitary matrix and Λ is a diagonal matrix. For birefringent optical elements constituting the metasurface, the diagonal matrix Λ determines their phase shifts δ_x and δ_y along the two perpendicular symmetry axes, while the matrix R determines the rotation angle θ of their fast axes relative to the reference coordinate in the x - y plane. (δ_x, δ_y) and θ determine the propagation phase and geometric phase imposed on the transmitted light, respectively. For the given spin-multiplexed phase profiles $\varphi_1(x, y)$ and $\varphi_2(x, y)$, the required phase shifts and rotation angle are calculated as (see Supplementary Note 3 for details):

$$\delta_x(x, y) = [\varphi_1(x, y) + \varphi_2(x, y)]/2 \quad (4)$$

$$\delta_y(x, y) = [\varphi_1(x, y) + \varphi_2(x, y)]/2 - \pi \quad (5)$$

$$\theta(x, y) = [\varphi_1(x, y) - \varphi_2(x, y)]/4 \quad (6)$$

Therefore, in order to implement $J(x, y)$, a series of subwavelength nanostructures are designed to provide the required phase shifts (δ_x, δ_y) covering the entire 2π phase range and satisfy the orientation angle θ at any point (x, y) . The metasurface design flow is summarized in Figure 2a. The propagation phase shifts δ_x and δ_y imparted by an individual nanopillar acting as a half-wave plate can be determined by its in-plane dimensions along the two perpendicular symmetry axes, and the geometric phase is controlled by orientation angle θ of the nanopillar. Combining them, the in-plane dimension and orientation of the nanopillars, of fixed height, constituting a vectorial metasurface can be determined at any point (x, y) on the metasurface plane.

Figure 2b shows a schematic diagram of metasurface composed of rectangular TiO₂ nanopillars on a fused-silica substrate with a subwavelength square lattice constant U . The nanopillars are of uniform heights H while their in-plane dimensions (D_x, D_y), and orientation angles θ vary spatially. In order to investigate the transmission properties of rectangular TiO₂ nanopillars, full-wave simulations are performed using the finite-difference time-domain (FDTD) technique. The height H of the TiO₂ nanopillars is set as 600 nm to achieve the desired 2π phase coverage. The lattice constant U is chosen to be 450 nm, which guarantees that the nanopillars array act as a zeroth order grating²² with relatively high transmission in the visible range. Supplementary Fig. S1 shows the simulated phase shifts and transmission coefficients of x - and y - polarized light for the rectangular nanopillars as a function of diameters (D_x, D_y) at a wavelength of $\lambda_0 = 530$ nm. Based on these simulation results, polarization conversion efficiencies of TiO₂ nanopillars are calculated and shown in the Figure 2c (see Supplementary Note 4 for details). A set of eight nanopillars, including four basic structures and four mirror structures are selected to provide eight phase levels covering the 2π phase range for δ_x and δ_y (Supplementary Fig. S2). The power transmission efficiency (T_x and T_y) and phase shifts (P_x and P_y) of eight nanopillars across the visible region are shown in Supplementary Fig.S3. As shown in Figure 2d, these geometrical parameters (Supplementary Table 1) are optimized such that the nanopillars' polarization conversion efficiencies are relatively high across the entire visible spectral range, which ensures broadband operation and efficient generation of POVs and PPBs. In addition, thanks to the high refractive index of the constituent material TiO₂, the optical fields at different wavelengths are all confined within individual nanopillars (Supplementary Fig. S4). This makes the TiO₂ nanopillar behave as a weakly coupled low-quality factor resonator, and thus validates the approximation of each nanopillar to be the local pixel of Jones matrix.

Generalized PPBs generated by the metasurfaces

Based on the above principle, two TiO₂ nanopillar metasurfaces (namely, MF1 and MF2) of area 90 μm × 90 μm are designed to generate two kinds of PPBs (PPB1 and PPB2). These two metasurfaces share the same device parameters: NA = 0.1, $f = 200$ μm, and $\gamma = 1.2$ at the design wavelength of $\lambda_0 = 530$ nm. PPB1 generated by MF1 is the superposition of two POVs with topological charge numbers ($l_{m,1} = 1, l_{n,1} = 5$) expressed by $\cos\frac{\alpha}{2}e^{i\beta/2}|\text{POV}_R, l = 1\rangle + \sin\frac{\alpha}{2}e^{-i\beta/2}|\text{POV}_L, l = 5\rangle$, while PPB2 generated by MF2 is the superposition of two POVs with topological charge numbers ($l_{m,2} = 5, l_{n,2} = 10$) expressed by $\cos\frac{\alpha}{2}e^{i\beta/2}|\text{POV}_R, l = 5\rangle + \sin\frac{\alpha}{2}e^{-i\beta/2}|\text{POV}_L, l = 10\rangle$. The independent spatial phase profiles for LCP and RCP light encoded onto the metasurface are shown in Supplementary Fig. S5. According to these spatial phase profiles, the phase shifts (δ_x, δ_y) and rotation angle θ of the birefringent TiO₂ nanopillars as a function of the spatial coordinates in the metasurface (MF1 and MF2) plane can be obtained and shown in Figure 2e.

Figure 2f shows the optical microscopy image and scanning electron microscopy (SEM) images of MF1 (Top) and MF2 (Bottom). The metasurface fabrication details are given in the Methods Section. Before the generation of PPBs, we first characterize the constituent spin-multiplexed optical vortices generated by the metasurfaces. By illuminating with RCP and LCP light generated from a supercontinuum laser attached to an acousto-optic tunable filter (AOTF) system, the in-plane (x - y plane) annular intensity distributions of the four generated optical vortices from MF1 ($|\text{POV}_R, 1\rangle, |\text{POV}_L, 5\rangle$) and MF2 ($|\text{POV}_R, 5\rangle, |\text{POV}_L, 10\rangle$) are captured at a step of 1 μm along the light propagation direction (z -axis). The top panel of Figure 3a shows the spatial intensities in the x - z plane of the generated optical vortices at the wavelength of $\lambda_0 = 530$ nm by stitching all the captured in-plane images together. It can be clearly seen that although the incident spin states and topological charges are all different for these two metasurfaces, the spatial patterns of the generated optical vortices along the propagation direction look very similar. The bottom panel of Figure 3a shows the measured annular intensity profiles of four optical vortices at the designed focal position $z = 200$ μm. As expected, four in-plane elliptical intensity profiles are almost identical. To better quantitatively evaluate the quality of the generated optical vortices, Figure 3b shows the cross sections of in-plane intensity profiles extracted from Figure 3a along the x - and the y -direction, respectively depicted by the white dashed and solid lines. At the designed wavelength of $\lambda_0 = 530$ nm, the vertical radius R_{\perp} , horizontal radius R_{\parallel} and ellipticity factor $\gamma = R_{\parallel}/R_{\perp}$ of the generated optical vortices are measured as following: for MF1, $R_{\parallel} = 24.3$ μm, $R_{\perp} = 19.9$ μm, $\gamma = 1.22$ for RCP and $R_{\parallel} = 25.1$ μm, $R_{\perp} = 20.9$ μm, $\gamma = 1.20$ for LCP; For MF2, $R_{\parallel} = 25.2$ μm, $R_{\perp} = 20.8$ μm, $\gamma = 1.21$ for RCP and $R_{\parallel} = 25.7$ μm, $R_{\perp} = 21.2$ μm, $\gamma = 1.21$ for LCP. The measured results are very close to the theoretical values of $R_{\parallel} = 24$ μm,

$R_{\perp} = 20 \mu\text{m}$, $\gamma = 1.20$. These results explicitly imply that the intensity profiles of the optical vortices generated by the metasurfaces are insensitive to the topological charge numbers, proving that they are POVs and thus can be used for the generation of PPBs. The experimentally measured generation efficiencies, defined as the ratio of the optical intensity of generated POVs to the intensity of the incident light, range between 50% and 54% for both MF1 and MF2 (see Supplementary Table 2).

In addition to the designed wavelength of 530 nm, thanks to the relatively high polarization conversion efficiency of the optimized nanopillars across the entire visible region, the metasurfaces exhibit a broadband response (see Supplementary Note 5 for details of broadband operation principle) and can also operate efficiently at other wavelengths. Figures 3c and 3d show the experimentally captured intensity profiles of the optical vortices generated by MF1 and MF2 at wavelengths of 480 nm (blue), 580 nm (yellow) and 630 nm (red). From the intensity profiles in the x - z plane (top panel of Figures 3c and 3d), as expected the focal length and NA of the metasurface are wavelength-dependent due to chromatic dispersion, however the optical vortices still exhibit very consistent spatial intensity distributions at these different wavelengths. At positions $z = 230 \mu\text{m}$, $195 \mu\text{m}$ and $180 \mu\text{m}$ respectively corresponding to blue, yellow and red light, the in-plane annular intensity patterns (bottom panel of Figures 3c and 3d) are almost identical to the one measured in green (Figure 3a). Therefore, the metasurfaces are still suitable for the generation of PPBs at other visible wavelengths. The cross sections of in-plane annular intensity profiles along x - and y - direction are given in Supplementary Fig. S11. The measured conversion efficiencies of these two metasurfaces for POVs at multiple wavelengths ranges from 31% to 45% (see Supplementary Table 2).

Next, to characterize these two metasurfaces for the generation of different PPBs, six points on the HyOPS are selected and their coordinates are given in Figure 4a. The corresponding polarization states of light (Figure 4b) incident on the metasurfaces are selected by rotating a quarter wave plate and a linear polarizer. The schematic of the experimental setup is illustrated in Supplementary Fig. S12. According to the topological charges of the constituent spin-multiplexed POVs, PPB1 and PPB2, generated from MF1 and MF2, respectively, have polarization order p and topological Pancharatnam charge l_p with $p_1 = (l_{m,1} - l_{n,1})/2 = -2$, $l_{p,1} = (l_{m,1} + l_{n,1})/2 = 3$ for PPB1, and $p_2 = (l_{m,2} - l_{n,2})/2 = -2.5$, $l_{p,2} = (l_{m,2} + l_{n,2})/2 = 7.5$ for PPB2. Figure 4c shows the experimental measured intensity patterns of PPB1 and PPB2 in the x - y plane at the focal position $z = 200 \mu\text{m}$ at a free-space wavelength of 530 nm. All the annular intensity patterns captured through a vertical linear polarizer for the two metasurfaces are of same contours, indicating that the radii of the generated PPBs are independent of sphere coordinate, polarization order and

topological Pancharatnam charge. As the polarization order p determines the number of polarization rotations per round trip, the lobe number of the PPB pattern can be derived as $2|p|$ from the anisotropic polarization distribution through a vertical polarizer. As shown in the second column to fifth column (Figure 4c), PPB1 and PPB2 are split into four and five lobes, respectively, which match well with the theoretical predictions of $p_1 = -2$ and $p_2 = -2.5$. In addition, we further confirm the anisotropic polarization distribution by Stokes polarimetry (see Supplementary Note 6 for details). The calculated and measured polarization distributions of the selected states corresponding to point II in Figure 4a for the two kinds of PPBs are shown in Figure 4d. It is clear that the polarization orientations rotate 4π and 5π per round trip for PPB1 and PPB2, respectively. The experimental results of these two PPBs agree well with the theoretical calculations (see Supplementary Note 7 for details and Supplementary Fig. S15 for calculated intensity patterns), except for a small rotation of the measured intensity and polarization patterns induced by the Gouy phase. In principle, the Gouy phase is dependent on the topological charge and can make the annular intensity pattern and polarization orientation distribution rotate by a small angle⁴⁸. As a consequence, this simple and efficient method to generate PPBs also offers a potential solution to visualize the Gouy phase experimentally.

Besides the operation wavelength of 530 nm, Figure 4e shows the experimental results for MF1 and MF2 illuminated at three other wavelengths across the visible region (480 nm, 580 nm and 630 nm). The intensity patterns for these illumination wavelengths are captured at $z = 230 \mu\text{m}$, $195 \mu\text{m}$ and $180 \mu\text{m}$, respectively. As expected, these lobed patterns exhibit very similar morphological characteristics as the one at a wavelength of 530 nm. Therefore, these results explicitly show that the metasurfaces can achieve efficient and broadband generation of PPBs in the visible region.

Optical information encryption

In the previous section, using a dielectric metasurface we have demonstrated the generation of PPBs that are independent of the topological charge number and polarization order. In principle, this approach encoding SAM and OAM states of light into PPBs in parallel channels can be employed for all-optical information encryption. For instance, various distinguishable PPBs with different polarization orders and ellipticities can be used to encode different double-digit hexadecimal numbers. For *e.g.*, if the absolute value of polarization order $|p|$ and ellipticity factor γ of the intensity pattern respectively denote the first and second digit of a double-digit hexadecimal number, and then a PPB represents a byte of data. As a result, the combination of 16 different values of $|p|$ and γ for the PPBs can represent 256 hexadecimal numbers from 00 to FF. In our design, polarization order $|p|$ ranging from 0 to 7.5 with an interval of 0.5 corresponds to the first hexadecimal digit from 0 to F, while

ellipticity factor γ ranging from 0.5 to 2.0 with an interval of 0.1 represents the second hexadecimal digit from 0 to F. This code chart is given in Supplementary Table 3 and can be used to denote the characters of various encoding schemes.

During the encryption, two states of perfect Poincaré beams' annular intensity images are combined to represent a double-digit hexadecimal number, which does not directly expose the encrypted information and increases the security. Anyone can access the original information only when he or she simultaneously possess all four indispensable hardware and software contents including metasurface device (ciphertext) as the encrypted information carrier, customized keys for acquisition of beam intensities, code chart for decrypting numbers and character encoding system for mapping numbers to plaintext composed of various characters. Although someone may steal the metasurface device and keys and capture the two kind of intensity patterns, they cannot decode the correct hexadecimal numbers without a code chart. Crucially, the code chart and character encoding system can be self-defined and not fixed. Therefore, it is almost impossible to access the information without accurate one-to-one mapping relationship. As a proof-of-concept demonstration, here we use American Standard Code for Information Interchange (ASCII) to implement the optical encoding and decoding for information encryption. User 1 wants to send a set of high-security account number and password to User 2 and translates the plaintext into the combinations of ASCII hexadecimal numbers as illustrated in Figure 5a. According to the hexadecimal numbers, 25 PPBs with the same $f = 200 \mu\text{m}$ and $\text{NA} = 0.1$ but different values of $|p|$ and γ are designed and encrypted on the metasurface, termed ciphertext (Figure 5b). Then User 1 sends the metasurface sample and a customized key to User 2. With the illumination of horizontal linearly polarized (LP) light at a wavelength of 530 nm on the metasurface, an image of PPBs array is captured with the filtration of a vertical linear polarizer (right panel of Figure 5c). Based on the code chart, the first hexadecimal digit can be determined by the lobe number of annular patterns. For instance, the first and last hexadecimal number in the text chart are respectively identified as "A" and "0", on the basis of the fact that light beam is spilt into 10 lobes on the top left corner and completely blocked on the bottom right corner. On the other side, when the metasurface is illuminated with LCP or RCP light (left panel of Figure 5c), another image of PPBs array without the filtration of a linear polarizer can be captured and the second hexadecimal digit can be determined by the ellipticity of annular patterns. For example, the first and last hexadecimal number in the text chart are respectively identified as "7" and "3" based on the annular beam with $\gamma = 1.2$ on the top left corner and another annular beam with $\gamma = 0.8$ on the bottom right corner. On the basis of this decoding rule, 25 double-digit hexadecimal numbers can be easily decrypted by the image identification. According to the ASCII (Supplementary Table 4), a customized program then converts the decrypted numbers into a string of ASCII characters including the account number and password information for User 2

to login on a computer (Figure 5d). In addition, this metasurface device also operates over a broad spectral range in the visible (see Supplementary Fig. S16) as evident from the intensity of PPB array at wavelengths of 480 nm, 580 nm and 630 nm which show similar patterns as the ones for the designed wavelength of 530 nm.

Conclusions

In conclusion, we have proposed and experimentally demonstrated broadband generation of perfect Poincaré beams via a single layer dielectric metasurface for visible light. By changing the spin angular momentum of incident light, the metasurface device with high spatial sampling resolution can generate spin-multiplexed perfect optical vortices with arbitrary orbital angular momentum. Via spatial superposition of two perfect optical vortices, different perfect Poincaré beams, whose total angular momenta are described by the hybrid-order Poincaré sphere, can be generated. Furthermore, based on the angular momenta states encoded within the generated perfect Poincaré beams, a proof-of-concept experimental demonstration for optical information encryption is implemented. We envision that this work will inspire creation of ultracompact flat nanophotonic elements for efficient generation and control of structured beams and further promote their practical applications, such as optical communication, optical encryption, optical data storage and quantum information sciences.

Methods

Numerical simulations:

Full-wave numerical simulations are performed using the finite-difference time-domain (FDTD) technique. Rectangular TiO₂ nanopillars with a fixed height of 600 nm are fabricated on a fused-silica substrate with a lattice constant of 450 nm. The incident plane-wave is polarized along x - or y - axes and illuminates the nanopillars from the substrate side. Along x and y axes, periodic boundary conditions are applied and perfectly matched layer (PML) boundary condition is used in the z direction. The phase shifts (P_x and P_y) and power transmission (T_x and T_y) (see Supplementary Fig. S1) are obtained by parameter sweeping of the in-plane dimensions (D_x and D_y) of the nanopillars by varying them between 50 nm and 350 nm at an interval of 5 nm.

Sample fabrication:

500 μm thick, double-side polished fused-silica substrates were first prime-vapor-coated with a monolayer of hexamethyldisilazane (HMDS) and then spin-coated with a layer of 600 nm thick positive-tone electron beam (e-beam) resist. Afterwards, the samples were coated with a layer of 10 nm thick aluminum (Al) via thermal evaporation, which suppressed the charging effect during the subsequent e-beam lithography step. E-beam lithography was performed at an accelerating voltage of 100 kV and beam current of 2 nA. The samples were developed in hexyl-acetate for 120 s. Next, the patterned samples were coated with TiO₂ using atomic layer deposition (ALD). The ALD was done at a low temperature of 90 °C to avoid deformation of the resist pattern. After the ALD, the overcoated TiO₂ layer was etched by the inductively-coupled-plasma reactive ion etching, with a gas mixture of Cl₂ and BCl₃. The etching was stopped when the overcoated TiO₂ has been fully removed and the e-beam resist was exposed. Finally, the samples were exposed to UV irradiation, followed by soaking in *n*-methyl-2-pyrrolidone, which removed the resist and produced the array of TiO₂ nanopillars with predesigned geometries.

Data availability

The data that support the findings of this study are available from the corresponding author upon reasonable request.

Reference

1. Born M., Emil, W. "Principles of Optics. Sixth (corrected) Edition." (1997).
2. Beth R.A. Mechanical Detection and Measurement of the Angular Momentum of Light. *Phys. Rev.* 50, 115-125 (1936).
3. Allen L., Beijersbergen M.W., Spreeuw R.J., Woerdman J.P. Orbital angular momentum of light and the transformation of Laguerre-Gaussian laser modes. *Phys. Rev. A* 45, 8185-8189 (1992).
4. O'Neil A.T., MacVicar I., Allen L., Padgett M.J. Intrinsic and extrinsic nature of the orbital angular momentum of a light beam. *Phys. Rev. Lett.* 88, 053601 (2002).
5. Yi, X., Liu, Y., Ling, X., Zhou, X., Ke, Y., Luo, H., Wen, S., Fan, D. Hybrid-order Poincaré sphere. *Phys. Rev. A* 91, (2015).
6. Poincaré H., *Theorie Mathematique de la Lumiere* (Gauthiers-Villars, Paris, 1892).
7. Milione G., Sztul H.I., Nolan D.A., Alfano R.R. Higher-Order Poincaré Sphere, Stokes Parameters, and the Angular Momentum of Light. *Phys. Rev. Lett.* 107, (2011).
8. Shen, Y., Wang, X., Xie, Z., Min, C., Fu, X., Liu, Q., Gong, M., Yuan, X. Optical vortices 30 years on: OAM manipulation from topological charge to multiple singularities. *Light Sci. Appl.* 8, 90 (2019).
9. Galvez, E. *Light Beams with Spatially-Variable Polarization*. Vol. 1, Chap. 3, 61 (2015).
10. Naidoo, D., Roux, F.S., Dudley, D., Litvin, I., Piccirillo, B., Marrucci, L., Forbes, A. Controlled generation of higher-order Poincaré sphere beams from a laser. *Nat. Photon.* 10, 327-332 (2016).
11. Rosales-Guzmán C, Ndagano B, Forbes A. A review of complex vector light fields and their applications. *Journal of Optics* 20, 123001 (2018).
12. Fang, X., Ren, H., Gu, M. Orbital angular momentum holography for high-security encryption. *Nat. Photon.* 14, 102–108 (2020).
13. Yan, H., Zhang, E., Zhao, B., Duan, K. Free-space propagation of guided optical vortices excited in an annular core fiber. *Opt. Express* 20, 17904-17915 (2012).
14. Niv A., Biener G., Kleiner V., Hasman E. Manipulation of the Pancharatnam phase in vectorial vortices. *Opt. Express* 14, 4208-4220 (2006).
15. Ostrovsky AS, Rickenstorff-Parrao C, Arrizon V. Generation of the "perfect" optical vortex using a liquid-crystal spatial light modulator. *Opt. Lett.* 38, 534-536 (2013).
16. Chen M, Mazilu M, Arita Y, Wright EM, Dholakia K. Dynamics of microparticles trapped in a perfect vortex beam. *Opt. Lett.* 38, 22 (2013).
17. Xu, R, Chen, P, Tang, J, Duan, W, Ge, S.-J, Ma, L.-L, Wu, R.-X, Hu, W, Lu, Y.-Q. Perfect Higher-Order Poincaré Sphere Beams from Digitalized Geometric Phases. *Phys. Rev. Appl.* 10, 034061 (2018).

18. Li, D., Feng, S., Nie, S., Chang, C., Ma, J., Yuan, C. Generation of arbitrary perfect Poincaré beams. *J. Appl. Phys.* 125, 073105 (2019).
19. Yu, N., Genevet, P., Kats, M.A., Aieta, F., Tetienne, J. P., Capasso, F., Gaburro, Z. Light propagation with phase discontinuities: generalized laws of reflection and refraction. *Science* 334, 333-337 (2011).
20. Kildishev, A.V., Boltasseva, A., Shalaev, V.M. Planar Photonics with Metasurfaces. *Science* 339, 1232009 (2013).
21. Lin, D., Fan, P., Hasman, E., and Brongersma, M. Dielectric gradient metasurface optical elements, *Science* 345, 298-302 (2014).
22. Arbabi A, Horie Y, Bagheri M, Faraon A. Dielectric metasurfaces for complete control of phase and polarization with subwavelength spatial resolution and high transmission. *Nat. Nanotechnol.* 10, 937-943 (2015).
23. Kruk S, Kivshar Y. Functional Meta-Optics and Nanophotonics Governed by Mie Resonances. *ACS Photon.* 4, 2638-2649 (2017).
24. Luo X. Engineering Optics 2.0: A Revolution in Optical Materials, Devices, and Systems. *ACS Photon.* 5, 4724-4738 (2018).
25. Wen D, Yue F, Liu W, Chen S, Chen X. Geometric Metasurfaces for Ultrathin Optical Devices. *Adv. Opt. Mater.* 6, 1800348 (2018).
26. Sun, S, He, Q, Hao, J, Xiao, S, Zhou, L. Electromagnetic metasurfaces: physics and applications. *Adv. Opt. Photonics* 11, 000380 (2019)
27. Cordaro, A., Kwon, H., Sounas, D., Koenderink, A. F., Alu A., Polman, A. High-index dielectric metasurfaces performing mathematical operations, *Nano Lett.* 19, 8418-8423 (2019).
28. Jiang, J., Fan, J.A. Global Optimization of Dielectric Metasurfaces Using a Physics-Driven Neural Network. *Nano Lett.* 19, 5366-5372 (2019).
29. Deng, Z. L., Jin, M., Ye, X., Wang, S., Shi, T.; Deng, J., Mao, N.; Cao, Y., Guan, B. O., Alù, A., Li, G., Li, X. Full-Color Complex-Amplitude Vectorial Holograms Based on Multi-Freedom Metasurfaces. *Adv. Funct. Mater.* 1910610 (2020).
30. Sroor, H., Huang, Y.W., Naidoo, D., Vallés, A., Ginis, V., Qiu, C.W., Antonio Ambrosio, Capasso, F., Forbes, A. High-purity orbital angular momentum states from a visible metasurface laser. *Nat. Photon.* (2020).
31. Khorasaninejad M, Capasso F. Metalenses: Versatile multifunctional photonic components. *Science* 358, 1146 (2017).
32. Wang, S., Wu, P. C., Su, V. C., Lai, Y. C., Chen, M. K, Kuo, H. Y, Chen, B. H, Chen, Y. H, Huang, T. T, Wang, J. H, Lin, R. M, Kuan, C. H, Li, T, Wang, Z, Zhu, S, Tsai, D. P. A broadband achromatic metalens in the visible. *Nat. Nanotechnol.* 13, 227-232 (2018).

33. Fan, Z. B., Qiu, H. Y., Zhang, H. L., Pang, X. N., Zhou, L. D., Liu, L., Ren, H., Wang, Q. H., Dong, J. W. A broadband achromatic metalens array for integral imaging in the visible. *Light Sci. Appl.* 8, 67 (2019).
34. Zhou, Y., Zheng, H., Kravchenko, I. and Valentine, J. Flat optics for image differentiation. *Nat. Photonics* 14, 316–323 (2020).
35. Huo, P., Zhang, C., Zhu, W., Liu, M., Zhang, S., Zhang, S., Chen, L., Lezec, H., Agrawal, A., Lu, Y. and Xu, T. Photonic spin-multiplexing metasurface for swichable spiral phase contrast imaging. *Nano. Lett.* 20, 2791-2798 (2020).
36. Bao, Y., Yu, Y., Xu, H., Guo, C., Li, J., Sun, S., Zhou, Z.K., Qiu, C.W., Wang, X.H. Full-colour nanoprint-hologram synchronous metasurface with arbitrary hue-saturation-brightness control. *Light Sci. Appl.* 8, 95 (2019).
37. Ren, H., Briere, G., Fang, X., Ni, P., Sawant, R., Heron, S., Chenot, S., Vezian, S., Damilano, B., Brandli, V., Maier, S. A., Genevet, P. Metasurface orbital angular momentum holography. *Nat. Commun.* 10, 2986 (2019).
38. Jin, L., Huang, Y. W., Jin, Z., Devlin, R. C., Dong, Z., Mei, S., Jiang, M., Chen, W. T., Wei, Z., Liu, H., Teng, J., Danner, A., Li, X., Xiao, S., Zhang, S., Yu, C., Yang, J. K. W., Capasso, F., Qiu, C. W. Dielectric multi-momentum meta-transformer in the visible. *Nat. Commun.* 10, 4789 (2019).
39. Li, G., Sartorello, G., Chen, S., Nicholls, L. H., Li, K. F., Zentgraf, T., Zhang, S., Zayats, A. V. Spin and Geometric Phase Control Four-Wave Mixing from Metasurfaces. *Laser Photonics Rev.* 12, 1800034 (2018).
40. Koshelev, K., Tang, Y., Li, K., Choi, D.Y., Li, G., Kivshar, Y. Nonlinear Metasurfaces Governed by Bound States in the Continuum. *ACS Photon.* 6, 1639-1644 (2019).
41. Devlin, RC, Ambrosio, A, Rubin, NA, Mueller, JPB, Capasso, F. Arbitrary spin-to-orbital angular momentum conversion of light. *Science* 358, 896-901 (2017).
42. Yue, F., Wen, D., Zhang, C., Gerardot, B. D., Wang, W., Zhang, S., Chen, X. Multichannel Polarization-Controllable Superpositions of Orbital Angular Momentum States. *Adv. Mater.* 29, 15 (2017).
43. Huo, P., Zhang S., Fan Q., Lu, Y., Xu, T. Photonic spin-controlled generation and transformation of 3D optical polarization topologies enabled by all-dielectric metasurfaces. *Nanoscale* 11, 10646-10654 (2019).
44. Zhang, Y., Liu, W., Gao, J., Yang, X. Generating Focused 3D Perfect Vortex Beams By Plasmonic Metasurfaces. *Adv. Opt. Mater.* 6, 1701228 (2018).
45. Bao, Y, Ni, J, Qiu, C.W. A Minimalist Single-Layer Metasurface for Arbitrary and Full Control of Vector Vortex Beams. *Adv. Mater.* 32, e1905659 (2020).
46. Mueller, J. P. B., Rubin, N. A., Devlin, R. C., Groever, B. & Capasso, F. Metasurface polarization optics: independent phase control of arbitrary orthogonal states of polarization. *Phys. Rev. Lett.* 118, 113901 (2017).

47. Ren, H., Shao, W., Li, Y., Salim, F., Gu, M. Three-dimensional vectorial holography based on machine learning inverse design. *Sci. Adv.* 6(16), eaaz4261 (2020)
48. Baumann, S.M., Kalb, D.M., MacMillan, L.H., Galvez, E.J. Propagation dynamics of optical vortices due to Gouy phase. *Opt. Express* 17, 9818-9827 (2009).

Acknowledgements

The work is supported by the Key Research and Development Program from Ministry of Science and Technology of China (2017YFA0303700 and 2016YFA0202100) and National Natural Science Foundation of China (11774163). W. Z., L. C. and A. A. acknowledge support under the Cooperative Research Agreement between the University of Maryland and the National Institute of Standards and Technology Center for Nanoscale Science and Technology, Award #70NANB14H209.

Author contributions

M. L., P. H., W. Z., C. Z. contributed equally. All authors contributed to the interpretation of results and participated in manuscript preparation.

Notes

The authors declare no competing interest.

Figure and caption

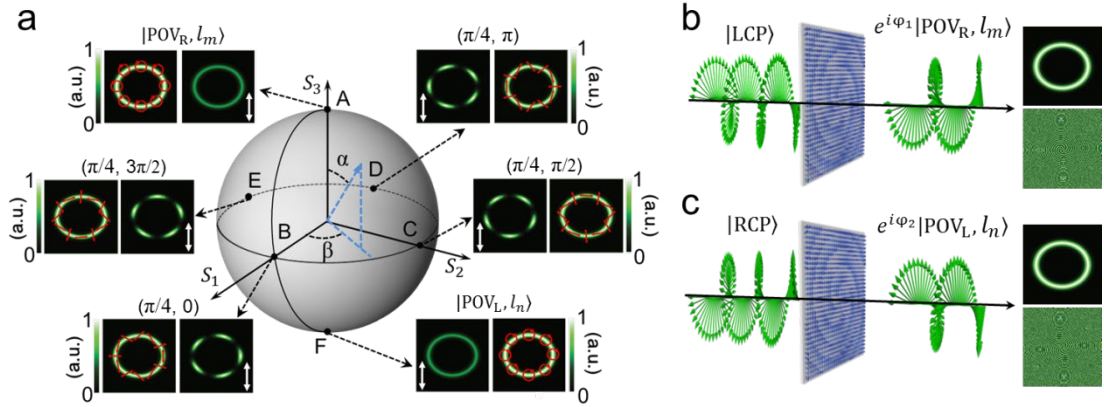


Figure 1. Principle of generation of generalized perfect Poincaré beams (PPBs) via dielectric metasurface. a A hybrid-order Poincaré Sphere (HyOPS) representation of various PPBs. As an example, the two poles are represented by two perfect vortices (POVs) with same ellipticity and different topological charges $l_m = 5$ and $l_n = 10$. The annular intensity profiles of six PPBs (red arrows represent the polarization distributions) with different coordinates are of same size and these elliptical hollow beams are transformed into distinct patterns using a vertical linear polarizer depicted by the white double arrow. **b, c** Left: Schematic illustration of the metasurface capable of providing two independent phase profiles φ_1 and φ_2 for LCP and RCP light, respectively. The output beam becomes a RCP (**b**) or LCP (**c**) POV with the topological charge of l_m (**b**) or l_n (**c**). Right: an example of the intensity (top) and phase (bottom) profiles of metasurface-generated POV with $l_m = 5$ (**b**) and $l_n = 10$ (**c**).

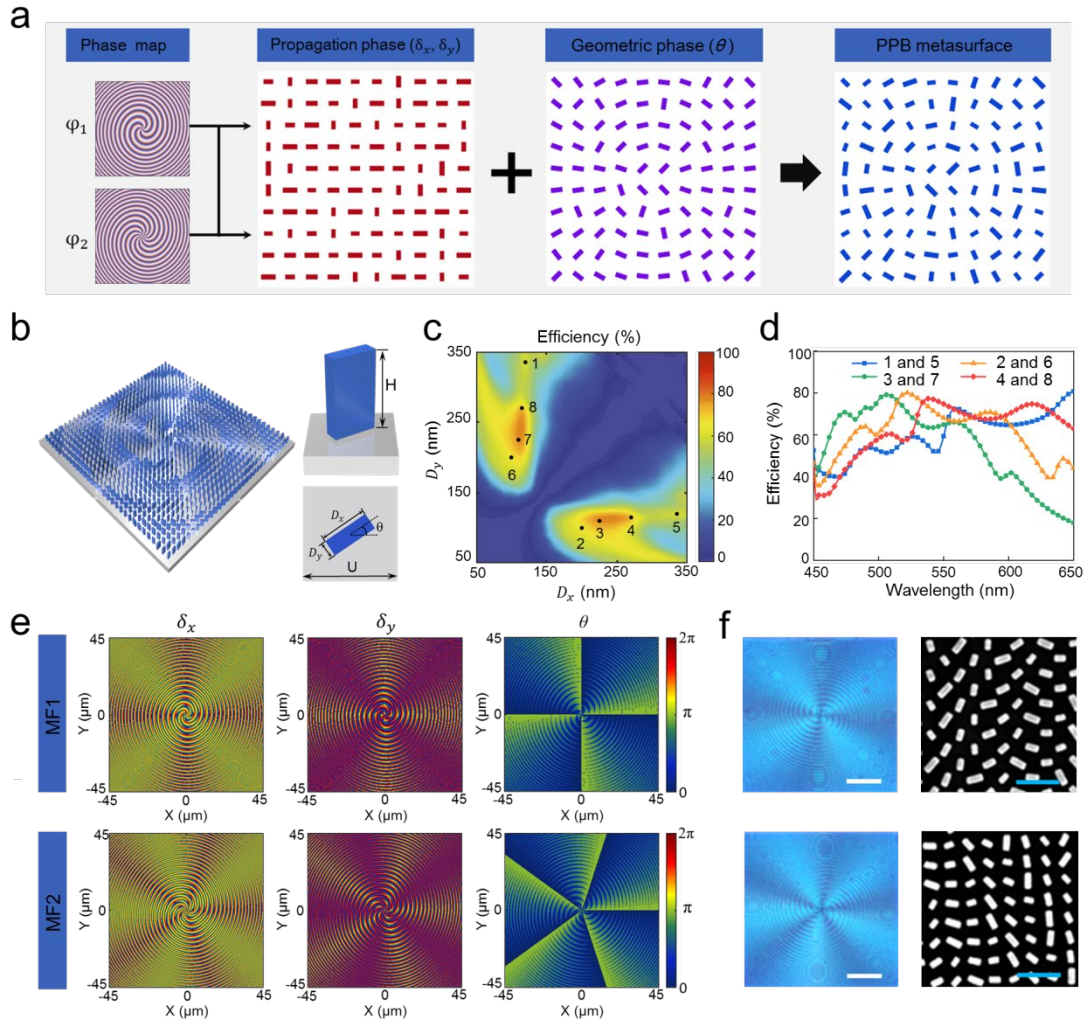


Figure 2. Design of a single layer metasurface. **a** A general metasurface design method to generate arbitrary PPB. Given two arbitrary phase maps (φ_1, φ_2) for generation of different perfect vortices, the phase shifts (δ_x, δ_y) and rotation angle θ of metasurface pixels are calculated and utilized to design nanopillars with varying in-plane dimensions and orientation angle. **b** Left: Schematic of the metasurface made up of TiO_2 rectangle nanopillars. Right: perspective view and top view of the unit cell arranged on a fused-silica substrate. **c** Calculated polarization conversion efficiency as a function of nanopillars' in-plane dimensions at a design wavelength of 530 nm. The black dots denote the selected nanopillars in constructing MF1 and MF2. **d** Calculated polarization conversion efficiencies of the selected eight nanopillars across the visible band. **e** The phase shifts (δ_x, δ_y) and rotation angle θ of the birefringent TiO_2 nanopillars as a function of the spatial coordinates in the metasurface (MF1 and MF2) plane. **f** Left: Optical microscope images of the fabricated metasurfaces: MF1 (Top) and MF2 (Bottom). Scale bar: 20 μm . Right: Top view scanning electron microscopy (SEM) images of metasurfaces. Scale bar: 500 nm.

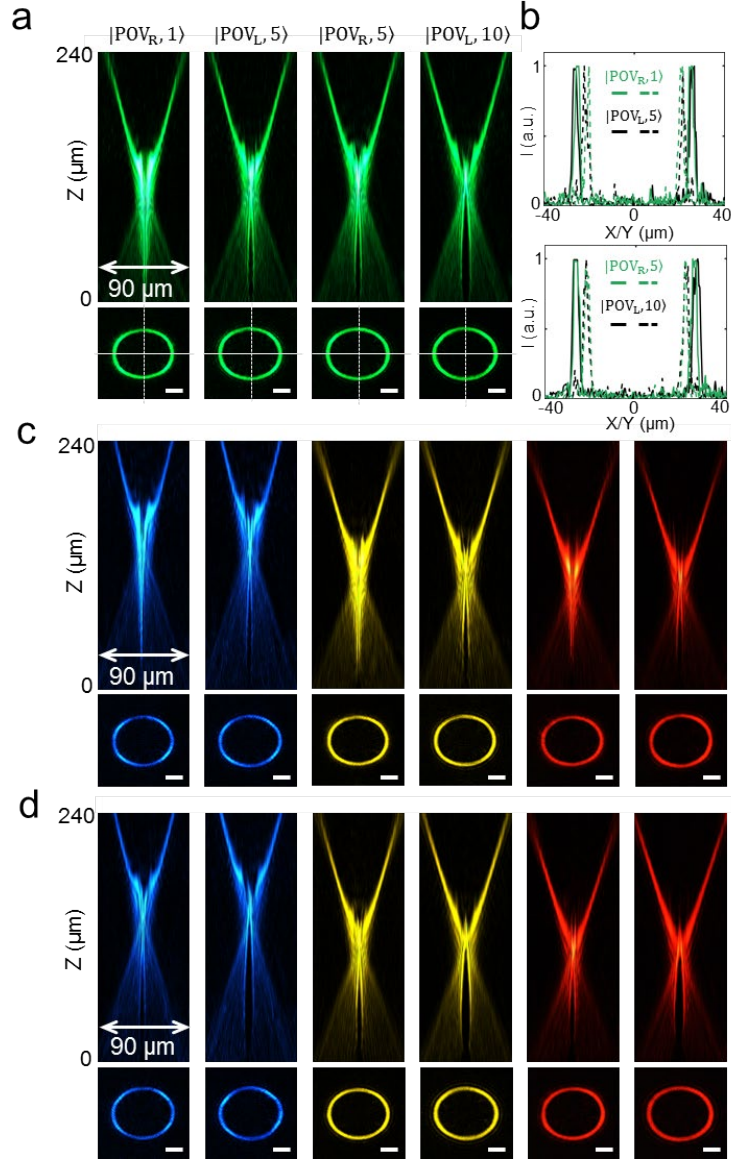


Figure 3. Characterization of metasurfaces for the generation of arbitrary POVs. **a** Top: measured intensity distributions of the four optical vortices with a linear scale in the y - z plane at a design wavelength of 530 nm: $|\text{POV}_{\text{R},1}\rangle$ and $|\text{POV}_{\text{L},5}\rangle$ corresponding to the metasurface MF1; $|\text{POV}_{\text{R},5}\rangle$ and $|\text{POV}_{\text{L},10}\rangle$ corresponding to the metasurface MF2. Bottom: measured annular intensity profiles of four optical vortices at the designed focal position $z = 200 \mu\text{m}$. Scale bar: 10 μm . **b** Normalized cross sections of the annular intensity profiles of the four optical vortices along the white dash and solid lines of **a** for MF1 (top) and MF2 (bottom). **c**, **d** Top: measured normalized intensity distributions of the optical vortices with a linear scale in the y - z plane at the wavelengths of 480 nm (blue), 580 nm (yellow) and 630 nm (red). Each wavelength corresponds to two orthogonally circular polarization optical vortices (**c**: $|\text{POV}_{\text{R},1}\rangle$ and $|\text{POV}_{\text{L},5}\rangle$ for metasurface MF1; **d**: $|\text{POV}_{\text{R},5}\rangle$ and $|\text{POV}_{\text{L},10}\rangle$ for metasurface MF2). Bottom: measured annular intensity profiles of optical vortices at the propagation distances $z = 230 \mu\text{m}$, $195 \mu\text{m}$ and $180 \mu\text{m}$ corresponding to the wavelengths of 480 nm (blue), 580 nm (yellow) and 630 nm (red). Scale bar: 10 μm .

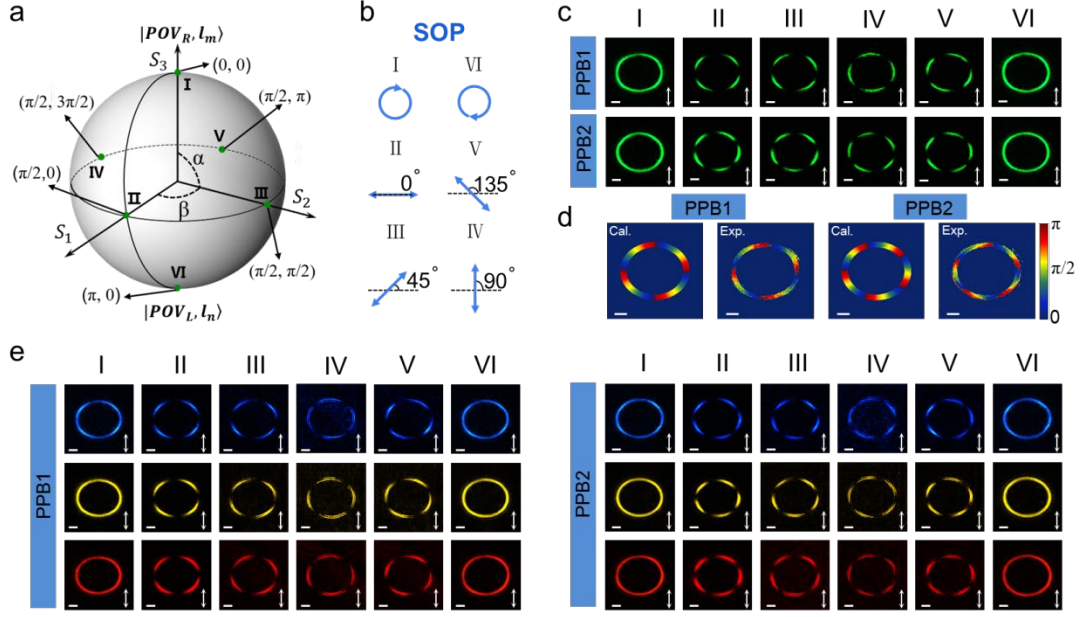


Figure 4. Evolutions of the metasurface-generated PPBs corresponding to the points on HyOPS. **a** The selected six points on HyOPS representing six states of PPBs generated successively by metasurface. **b** Six states of polarization (SOP) of the light incident on the metasurfaces are chosen to generate various states of PPBs corresponding to the coordinates in **a**. **c** The measured annular intensity patterns of the output states corresponding to the points in **a** for PPB1 and PPB2 in the x - y plane after transmission through a vertical linear polarizer depicted by the white double arrow. These images are captured at the designed focal position $z = 200 \mu\text{m}$. Scale bar: $10 \mu\text{m}$. **d** The calculated and measured polarization orientations and distributions of PPB1 and PPB2 corresponding to point II in **a**. Note that the horizontal polarization orientation is defined as 0 rad . Scale bar: $10 \mu\text{m}$. **e** Measured annular intensity patterns of the PPB1 and PPB2 in the x - y plane at the wavelengths of 480 nm (blue), 580 nm (yellow) and 630 nm (red) at a propagation distance of $z = 230 \mu\text{m}$, $195 \mu\text{m}$ and $180 \mu\text{m}$. These images are captured through a linear polarizer depicted by the white double arrow. Scale bar: $10 \mu\text{m}$.

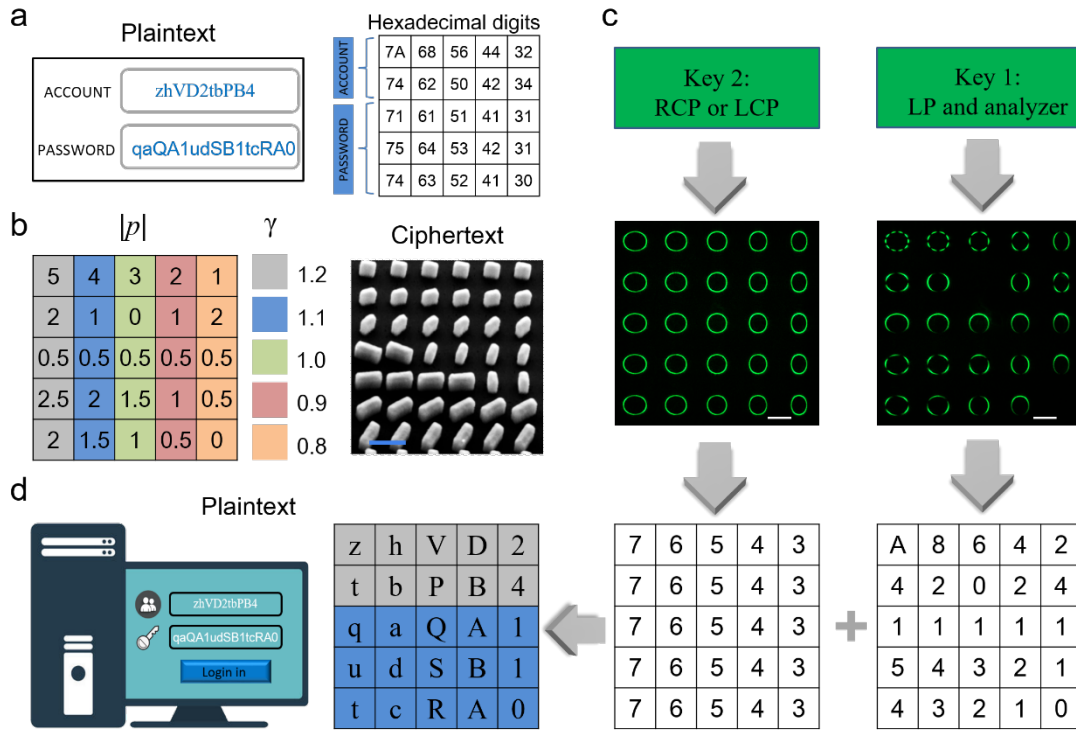


Figure 5. Proof-of-concept experimental demonstration of optical information encryption. **a** The plaintext message including a set of complex account number and password composed of different characters (left) are translated into the combinations of hexadecimal numbers (right) by User 1. **b** The design parameters of the 25 PPBs (left) and SEM image of a portion of the metasurface termed ciphertext (right). Scale bar: 500 nm. **c** User 2 captures two images with the two customized keys. According to the code chart, the first and second digits of these two-digit hexadecimal numbers are decrypted by User 2, respectively. Scale bar: 50 μ m. **d** The hexadecimal number combination is decrypted as the plaintext message including the account number and password based on the ASCII.

Supplementary for Broadband generation of perfect Poincaré beams via dielectric spin-multiplexed metasurface for optical information encryption

Mingze Liu^{1,2}, Pengcheng Huo^{1,2}, Wenqi Zhu^{3,4}, Cheng Zhang⁵, Si Zhang^{1,2}, Maowen Song^{1,2}, Song Zhang^{1,2}, Qianwei Zhou^{1,2}, Lu Chen^{3,4}, Henri J. Lezec³, Amit Agrawal^{3,4}, Yanqing Lu^{1,2} and Ting Xu^{1,2}

1. National Laboratory of Solid-State Microstructures, Jiangsu Key Laboratory of Artificial Functional Materials, College of Engineering and Applied Sciences, Nanjing University, Nanjing 210093, China
2. Collaborative Innovation Center of Advanced Microstructures, Nanjing 210093, China
3. Physical Measurement Laboratory, National Institute of Standards and Technology, Gaithersburg, Maryland 20899, United States
4. Maryland NanoCenter, University of Maryland, College Park, Maryland 20899, United States
5. School of Optical and Electronic Information, Wuhan National Laboratory for Optoelectronics, Huazhong University of Science and Technology, Wuhan 430074, China.

Supplementary Note 1. Derivation of POV using the Fourier transform of higher-order Bessel beam.

In theory, a POV can be generated by the Fourier transform of a higher-order Bessel beam¹. Because it is nontrivial to generate an ideal Bessel beam experimentally, we consider a Bessel-Gaussian beam which can be generated by passing a Gaussian beam through an axicon. The complex field amplitude of a Bessel-Gaussian beam with uniform circular polarization in the cylindrical coordinate system (ρ, ϕ, z) is expressed as²:

$$\vec{E}(\rho, \phi, z) = J_l(k_r \rho) \exp(il\phi) \exp(ik_z z) \exp\left(-\frac{\rho^2}{\omega_g}\right) \begin{bmatrix} 1 \\ \pm i \end{bmatrix} \quad (\text{S1})$$

where J_l is an l -th order Bessel function of the first kind, k_r and k_z are the radial and longitudinal wavevectors and ω_g is the waist of the Gaussian beam. The Fourier transform of the Bessel-Gaussian beam can be implemented by an optical lens. The Fourier transformation of the optical field $\vec{E}(\rho, \phi)$ into $\vec{E}(r, \varphi)$ is expressed as³:

$$\vec{E}(r, \varphi) = \frac{k}{i2\pi f} \int_0^\infty \int_0^{2\pi} \vec{E}(\rho, \phi) \rho \exp\left[-\frac{ik\rho r \cos(\varphi - \phi)}{f}\right] d\rho d\phi \quad (\text{S2})$$

where f is the focal length of lens. By substituting eq. S1 into eq. S2, the complex field amplitude of the POV in the focal plane is obtained as:

$$\vec{E}(r, \varphi) = \frac{\omega_g i^{l-1}}{\omega_\gamma} \exp(il\varphi) I_l\left(\frac{2R_\gamma r}{\omega_\gamma^2}\right) \exp\left(\frac{-r^2 - R_\gamma^2}{\omega_\gamma^2}\right) \begin{bmatrix} 1 \\ \pm i \end{bmatrix} \quad (\text{S3})$$

where I_l is an l -th order modified Bessel function of the first kind, $r = \sqrt{(x)^2 + (y\gamma)^2}$, $\varphi = \text{atan}(\gamma y/x)$, $R_\gamma = \gamma k_r f/k$, γ is a scale factor and controls the ellipticity of POV, (x, y) are Cartesian coordinates in the rear focal plane of the lens, $R_\gamma = \gamma k_r f/k$, $k = 2\pi/\lambda$ is the wave vector, f is the focal length of the lens, k_r can be controlled by the numerical aperture of the axicon NA, and $\omega_\gamma = 2\gamma f/k\omega_g$ is waist of Gaussian beam at the rear focal plane of the lens. For small ω_γ at the focus of the lens and large R_γ , $I_l\left(\frac{2R_\gamma r}{\omega_\gamma^2}\right)$ can be approximated as $\exp\left(\frac{2R_\gamma r}{\omega_\gamma^2}\right)$. Eq. S3 can be rewritten as:

$$\vec{E}(r, \varphi) = \frac{\omega_g i^{l-1}}{\omega_\gamma} \exp(il\varphi) \exp\left(\frac{-(r - R_\gamma)^2}{\omega_\gamma^2}\right) \begin{bmatrix} 1 \\ \pm i \end{bmatrix} \quad (\text{S4})$$

Note that the amplitude of the POV is shaped by a Gaussian function with a maximum intensity at $r = R_\gamma$. The radius of the POV along the vertical and horizontal directions are $R_\perp = fNA$ and $R_\parallel = \gamma fNA$, which are both independent of topological charges.

Supplementary Note 2. Phase distributions of the metasurface for generation of PPBs

As shown in the main text, the PPBs are composed of orthogonal circularly polarized POVs, and the POVs can be generated by the Fourier transformation of a higher-order Bessel-Gaussian beam. In the experiments, a Gaussian beam can become POV after successively passing through a spiral phase plate, axicon and Fourier transformation lens. A metasurface can implement this multielement multifunctional process for either RCP or LCP incident light by satisfying the superposition of the phase distributions of a spiral phase plate $\varphi_{spiral}(x, y)$, an axicon $\varphi_{axicon}(x, y)$ and a Fourier transformation lens $\varphi_{lens}(x, y)$ which are expressed as:

$$\varphi_{spiral}(x, y) = l \cdot \arctan(y/\gamma x) \quad (S5)$$

$$\varphi_{axicon}(x, y) = -\frac{2\pi}{\lambda} \sqrt{(\gamma x)^2 + (y)^2} \cdot \text{NA} \quad (S6)$$

$$\varphi_{lens}(x, y) = -\frac{\pi}{\lambda f} (x^2 + y^2) \quad (S7)$$

where (x, y) is the geometric coordinate of the metasurface and $l = l_m$ or l_n for RCP or LCP light respectively. Thus the phase profile $\varphi_{meta}(x, y) = \varphi_1(x, y)$ or $\varphi_2(x, y)$ encoded respectively on the metasurface for RCP or LCP light is described as:

$$\varphi_{meta}(x, y) = \varphi_{spiral}(x, y) + \varphi_{axicon}(x, y) + \varphi_{lens}(x, y) \quad (S8)$$

Supplementary Note 3. Derivation of the Jones matrix J and its eigenvalues and eigenvectors:

An arbitrary polarized light beam normally incident onto the metasurface can be decomposed into RCP and LCP spin eigenstates with corresponding two-dimensional (2D) Jones vectors given by: $|\text{LCP}\rangle = \begin{bmatrix} 1 \\ i \end{bmatrix}$ and $|\text{RCP}\rangle = \begin{bmatrix} 1 \\ -i \end{bmatrix}$. In order to generate two completely different POVs represented by two poles of the HyOPS, the metasurface is required to provide two independent spatial phase profiles $\varphi_1(x, y)$ and $\varphi_2(x, y)$ corresponding to $|\text{LCP}\rangle$ and $|\text{RCP}\rangle$, where $\varphi_1(x, y)$ and $\varphi_2(x, y)$ are the superposition of the phase distributions of the spiral phase plate, axicon and Fourier transform lens. That is, for LCP incident light, the metasurface can implement the transformation: $|\text{LCP}\rangle \rightarrow |\text{POV}_R, l_m\rangle$ (Figure 1b). The output beam $|\text{POV}_R, l_m\rangle$ will have opposite handedness compared to the incident beam. Similarly, the same metasurface can also transform RCP incident light to a different POV with LCP state and topological charge of l_n : $|\text{RCP}\rangle \rightarrow |\text{POV}_L, l_n\rangle$ (Figure 1c). The metasurface can be described by a Jones matrix $J(x, y)$ which simultaneously satisfies $J(x, y)|\text{LCP}\rangle = \exp[i\varphi_1(x, y)]|\text{RCP}\rangle$ and $J(x, y)|\text{RCP}\rangle = \exp[i\varphi_2(x, y)]|\text{LCP}\rangle$ at each point (x, y) . Matrix inversion of these two equations results in:

$$J(x, y) = \begin{bmatrix} \exp[i\varphi_1(x, y)] & \exp[i\varphi_2(x, y)] \\ -i\exp[i\varphi_1(x, y)] & i\exp[i\varphi_2(x, y)] \end{bmatrix} \begin{bmatrix} 1 & 1 \\ i & -i \end{bmatrix}^{-1} \quad (\text{S9})$$

The required Jones matrix is calculated as:

$$J(x, y) = \begin{bmatrix} \frac{\exp[i\varphi_1(x, y)] + \exp[i\varphi_2(x, y)]}{2} & \frac{i\exp[i\varphi_2(x, y)] - i\exp[i\varphi_1(x, y)]}{2} \\ \frac{i\exp[i\varphi_2(x, y)] - i\exp[i\varphi_1(x, y)]}{2} & \frac{-\exp[i\varphi_1(x, y)] - \exp[i\varphi_2(x, y)]}{2} \end{bmatrix} \quad (\text{S10})$$

Due to symmetric and unitary conditions, $J(x, y)$ can be written in a standard form $J(x, y) = R\Lambda R^{-1}$, where R is a real unitary matrix and Λ is a diagonal matrix. By solving the characteristic equation of $J(x, y)$, its eigenvalues are calculated as:

$$\lambda_1 = e^{i\frac{1}{2}[\varphi_1(x, y) + \varphi_2(x, y)]} \quad \lambda_2 = e^{i\frac{1}{2}[\varphi_1(x, y) + \varphi_2(x, y)] - i\pi} \quad (\text{S11})$$

and eigenvectors as:

$$V_1 = [\cos \theta \quad \sin \theta]^T \quad V_2 = [-\sin \theta \quad \cos \theta]^T \quad (\text{S12})$$

where $\theta = \frac{1}{4}[\varphi_1(x, y) - \varphi_2(x, y)]$. Thus, the Jones matrix can be rewritten in terms of its eigenvectors and eigenvalue as:

$$J(x, y) = R\Lambda R^{-1} = [V_1 \quad V_2] \begin{bmatrix} \lambda_1 & 0 \\ 0 & \lambda_2 \end{bmatrix} [V_1 \quad V_2]^{-1} \quad (\text{S13})$$

Since the matrix $J(x, y)$ operates in the linear polarization basis, the diagonal matrix Λ determines the phase shifts $\delta_x = \frac{1}{2}[\varphi_1(x, y) + \varphi_2(x, y)]$ and $\delta_y = \frac{1}{2}[\varphi_1(x, y) + \varphi_2(x, y)] - \pi$ along the two symmetry axes of the linearly birefringent element. Meanwhile, the matrix R corresponds to a rotation matrix for Λ and determines the rotation angle $\theta = \frac{1}{4}[\varphi_1(x, y) - \varphi_2(x, y)]$ of the fast axis of the birefringent element in the x - y plane. In order to implement $J(x, y)$, a series of sub-wavelength nanopillars are designed to provide the required phase shifts (δ_x, δ_y) covering an entire 2π phase range and satisfying the orientation angle (θ) requirement at any point (x, y) of the metasurface.

Supplementary Note 4. Calculation of polarization conversion efficiency of the unit cells.

For an arbitrary polarized light $|E_{in}\rangle$ incident on the metasurface unit cell, the transmitted light $|E_{out}\rangle$ can be expressed as⁴:

$$|E_{out}\rangle = \eta_E |E_{in}\rangle + \eta_R e^{i2\theta} |\text{RCP}\rangle + \eta_L e^{-i2\theta} |\text{LCP}\rangle \quad (\text{S14})$$

where $\eta_E = \frac{1}{2}(T_x + T_y e^{i\xi})$, $\eta_R = \frac{1}{2}(T_x - T_y e^{i\xi})\langle E_{in}|\text{LCP}\rangle$ and $\eta_L = \frac{1}{2}(T_x - T_y e^{i\xi})\langle E_{in}|\text{RCP}\rangle$ represent the transmission coefficients of different polarization orders and θ is the orientation of the fast axis of the metasurface unit cell. Here, $\langle E_{in}|\text{RCP or LCP}\rangle$ is an inner product. T_x and T_y are the spectral transmission coefficients of the unit-cell for light polarized parallel and perpendicular to the fast axis and ξ is the phase difference between T_x and T_y . For an incident light with circular polarization ($|\text{LCP}\rangle$ or $|\text{RCP}\rangle$), the polarization conversion efficiency η_R^2 or η_L^2 can be obtained according to the eq. S14 as:

$$\eta_R^2 = \left| \frac{1}{2}(T_x - T_y e^{i\xi})\langle E_{in}|\text{LCP}\rangle \right|^2 \quad (\text{S15})$$

$$\eta_L^2 = \left| \frac{1}{2}(T_x - T_y e^{i\xi})\langle E_{in}|\text{RCP}\rangle \right|^2 \quad (\text{S16})$$

Supplementary Note 5. Broadband response for the proposed metasurface

As for broadband response, the proposed metasurface composed of sub-wavelength nanopillars has a broadband phase modulation of two orthogonal circular polarization states. The geometric phase is wavelength-insensitive and each metasurface nanopillar with same orientation angle can impart same geometric phase value at various wavelengths. Meanwhile, the broadband-response propagation phases with same linear gradients imparted by a group of eight selected metasurface nanopillars can always cover the entire 0 to 2π phase range at various wavelengths. The two broadband phase modulations ensure that the proposed metasurface can completely offer RCP or LCP phase profiles with very similar contours at wavelengths of 480 nm, 530 nm, 580 nm and 630 nm, respectively. Therefore, the metasurface-offered broadband RCP and LCP phase profiles can achieve broadband generation of orthogonal circular polarized perfect vortices and perfect Poincaré beams. However, due to the existence of chromatic dispersion, the beam size and divergence angles of perfect vortices and perfect Poincaré beams are not identical for various incident wavelengths.

To further analyze and explain broadband generation of perfect Poincaré beams achieved here, we must quantitatively clarify the phase response achieved from the metasurface for two orthogonal circular polarization states at different incident wavelengths. In terms of the metasurface nanopillars' phase modulation used in this paper, the geometric phase depends only on the geometry of the pathway through the anisotropy transforming the light wave and is wavelength-insensitive. Specifically, each metasurface nanopillar acting as a half waveplate with same orientation angle (θ) can offer same PB phase ($\varphi_{PB} = 2\theta$) of the output wavefront at various wavelengths. Then, we simulated the geometric phases of eight nanopillars chosen for this study with a certain orientation angle at different wavelengths. As an example, Supplementary Fig. S6 shows the simulated geometric phases of eight selected nanopillars with same orientation angle of $\pi/2$ when illuminating circularly polarized light at wavelengths of 480 nm, 530 nm, 580 nm and 630 nm. The simulated geometric phases of cross-polarized output wavefronts at various wavelengths are consistent with the theoretical values (Supplementary Fig. S6) of π and thus the geometric phase is wavelength-insensitive.

As for the propagation phase, it is accumulated through light wave propagating in the nanopillar behaving as a truncated waveguide, which can be expressed as:

$$\varphi_{PG}(\lambda) = (2\pi/\lambda) n_e H \quad (\text{S17})$$

where λ is the wavelength of incident light, n_e is the effective refractive index of propagating optical mode which depends on the lateral size of the TiO₂ nanopillar and its surroundings medium (air), and H is the height of the nanopillar. Because the refractive index of TiO₂ nanopillar is relatively flat in the visible between wavelengths of 450 nm and 650 nm (Supplementary Fig. S7), the effective refractive index n_e basically depends on the size of TiO₂ nanopillar and is approximately wavelength-independent. Theoretically, the propagation phase shift $\varphi_{constant}(\lambda)$ of a nanopillar between the designed wavelength (λ_0) and another wavelength (λ) is proportional to $(\frac{1}{\lambda} - \frac{1}{\lambda_0})$. Supplementary Fig. S8a shows the theoretical propagation phase offered by the set of eight nanopillars chosen for this study at different incident wavelengths of 480 nm, 580 nm and 630 nm. These phases, all offer the same linear gradient at various wavelengths can cover the requisite full 2π phase range. To further verify the above theoretical analysis, we simulated and calculated the phase of complex polarization conversion coefficient of $(t_x - t_y)/2$ for the eight selected nanopillars at different incident wavelength of 480 nm, 530 nm, 580 nm and 630 nm (Supplementary Fig. S8b), where t_x and t_y represent complex transmission coefficients for x - and y - polarized light incident on the nanopillar, respectively. The phase part of complex polarization conversion coefficient which is the propagation phase offered by the eight nanopillars can cover the entire 0 to 2π phase range at the design wavelength of 530nm as well as at other wavelengths of 480 nm, 580 nm and 630 nm. The simulated propagation phases accord closely with the theoretical propagation phases. In addition, the relatively constant propagation phase differences of each nanopillar between the designed wavelength ($\lambda_0 = 530$ nm) and other incident wavelengths ($\lambda = 480$ nm, 580 nm or 630 nm) can't disorganize the entire in-plane phase distributions for RCP and LCP light offered by the proposed metasurface at various wavelengths (discussed in next paragraph).

Meanwhile, the phase profiles imparted by the broadband metasurface for RCP or LCP light at a specific wavelength can be expressed as:

$$\varphi_{RCP/LCP}(\lambda, x, y) = \varphi_{PG}(\lambda, x, y) \pm \varphi_{PB}(x, y) \quad (\text{S18})$$

where $\varphi_{PG}(\lambda, x, y)$ is the propagation phase accrued upon propagation through a TiO₂ nanopillar for different wavelengths at any point (x, y) of the metasurface, $\varphi_{PB}(x, y)$ is geometric phase and equals $2\theta(x, y)$ where $\theta(x, y)$ is the in-plane rotation angle of a TiO₂ nanopillar at any point (x, y) of the metasurface. Considering phase modulation mechanism, the exact geometric phase and propagation phase imparted by each metasurface nanopillar at different wavelengths, as an example, the theoretical and simulated phase profiles for both RCP and LCP light offered by a metasurface for generation of two orthogonal circularly polarized perfect vortices at wavelengths of 480 nm, 530 nm, 580 nm and 630 nm are given in Supplementary Fig. S9. The in-plane phase profiles for RCP and LCP light are normalized to 0 to 2π range. The metasurface parameters are as follows: two topological charges l_m of 5 and l_n of 10, ellipticity factor γ of 1.2, focal length f of 200 μm , numerical aperture NA of 0.1 and designed wavelength λ_0 of 530 nm. The theoretical phase profiles (Supplementary Fig. S9a) for RCP and LCP light at each wavelength maintains the same contour, respectively, which arises from the same $\varphi_{constant}(\lambda)$ for the eight nanopillars at a specific wavelength λ . The simulated phase profiles (Supplementary Fig. S9b) for RCP and LCP light are well matched with the theoretical results. This indicates that the proposed metasurface can achieve broadband generation of two orthogonal circularly polarized perfect vortices because of its broadband phase response for RCP and LCP light.

In order to see the phase shifts between design wavelength and other wavelengths more clearly, the cross sections of these in-plane phase profiles are extracted from Supplementary Fig. S9 along x -axis depicted by dashed white lines and unwrapped, as shown in Supplementary Fig. S10. The simulated results also agree well with the theoretical results.

Supplementary Note 6. Stokes polarimetry of PPBs and spherical wave interferometry

The polarization state of PPBs on the HyOPS is mapped by representing the Stokes parameters in the spherical Cartesian coordinates. Stokes polarimetry is implemented by measuring a series of intensity distributions to obtain the values of Stokes parameters expressed as⁵:

$$S_0 = I_0 + I_{90} \quad (\text{S19})$$

$$S_1 = I_0 - I_{90} \quad (\text{S20})$$

$$S_2 = I_{45} - I_{135} \quad (\text{S21})$$

$$S_3 = I_R - I_L \quad (\text{S22})$$

where I_0 , I_{45} , I_{90} and I_{135} are the intensities of PPBs after transmission through a rotated linear polarizer oriented at 0° , 45° , 90° and 145° with respect to the x -axis respectively. I_R and I_L are the intensities of PPBs after transmission through a right and a left circular polarizer, respectively. In order to reduce the numbers of measurements, I_{135} and I_L can be expressed as: $I_{135} = I_0 + I_{90} - I_{45}$; $I_L = I_0 + I_{90} - I_R$. Therefore, all the Stokes parameters can be obtained by measuring four intensity distributions (I_0 , I_{45} , I_{90} and I_R) through the PPBs. The spherical coordinates (α, β) of the points on the HyOPS can be determined by the Stokes parameters: $\alpha = \arccos\left(\frac{S_3}{S_0}\right)$ and $\beta = \arctan\left(\frac{S_2}{S_1}\right)$. Thus, the spatial distribution of polarization orientation angle θ for the PPB described by any point on the HyOPS can be obtained as:

$$\theta = \frac{1}{2} \arctan\left(\frac{S_2}{S_1}\right) \quad (\text{S23})$$

In order to analyze the polarization distribution of the PPBs in experiment, a linear polarizer and a quarter waveplate are inserted at the front of the camera to measure these four intensities distributions (I_0 , I_{45} , I_{90} and I_R). In addition, in order to accurately distinguish state A and state F in Figure 1a, Stokes polarimetry and spherical wave interferometry should be performed on the two beams, respectively. First, a measurement of four intensities (I_0 , I_{45} , I_{90} and I_R) of the two beams after transmission through a quarter waveplate and a linear polarizer must be performed. According to these intensities (Supplementary Fig. S13), one

can calculate the spherical coordinates (α, β) of the two beams corresponding to the point on the HyOPS: for state A, the spherical coordinates is $(0, 0)$ which corresponds to RCP perfect vortex; for state F, the spherical coordinates is $(\pi, 0)$ which corresponds to LCP perfect vortex. Furthermore, to determine the topological charge of the perfect vortex, the RCP or LCP spherical wave is interfered with RCP or LCP perfect vortex. The simulated interference patterns are shown in Supplementary Fig. S14. According to the number of lobes, one can determine the topological charges of RCP and LCP perfect vortex to be 5 and 10, respectively. Therefore, using the measurement sequence outlined above, one can distinguish state A from state F and accurately determine the polarization distribution and topological charges of the two beams. As for the measurement of other states on the HyOPS, Stokes polarimetry only needs to be implemented for these beams.

Supplementary Note 7. Intensity calculation for PPBs with superpositions of POVs

According to the eq. S4, the magnitude of a POV with topological charge l is expressed as:

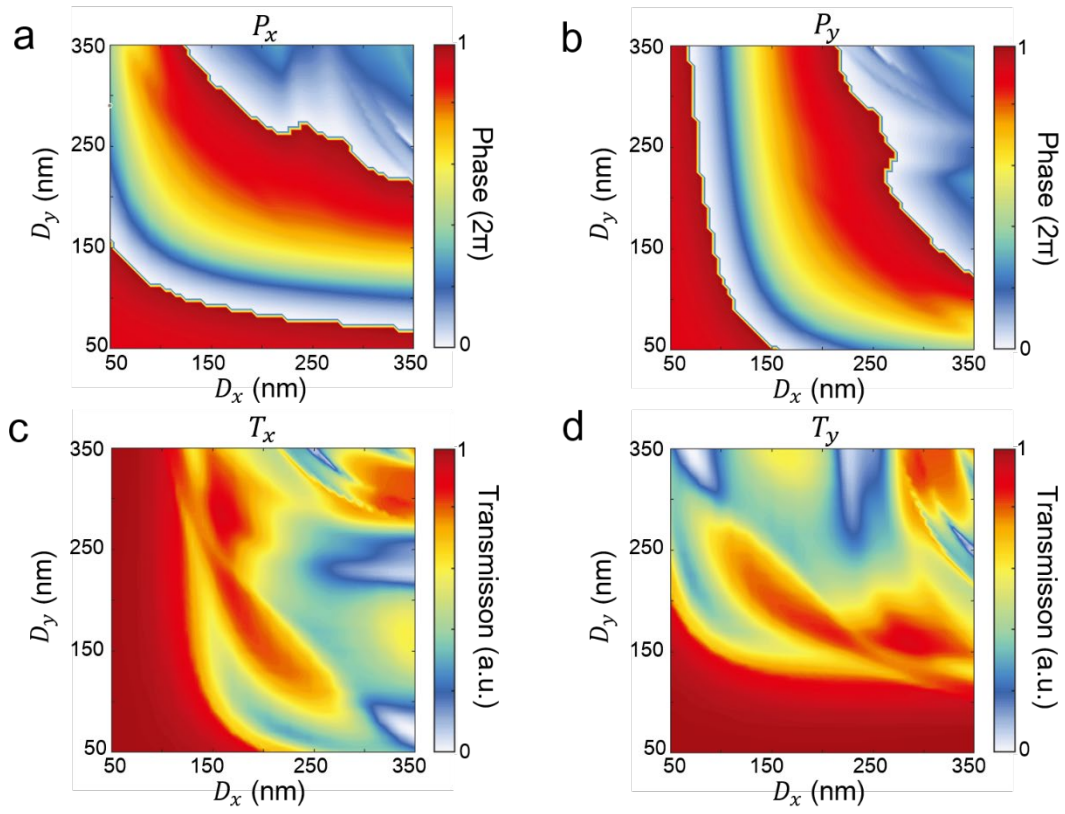
$$E_l(r, \varphi) = \frac{\omega_g i^{l-1}}{\omega_\gamma} \exp(il\varphi) \exp\left(-\frac{(r-R_\gamma)^2}{\omega_\gamma^2}\right) \quad (\text{S24})$$

As shown in the main text, the PPB is the superposition of two orthogonal circular polarization POVs. For an arbitrary polarization state of light incident on the metasurface device, the output light is a superposition of the form given by eq. 1. The intensity of the output PPB corresponding to point (α, β) on the HyOPS is calculated by the following equation:

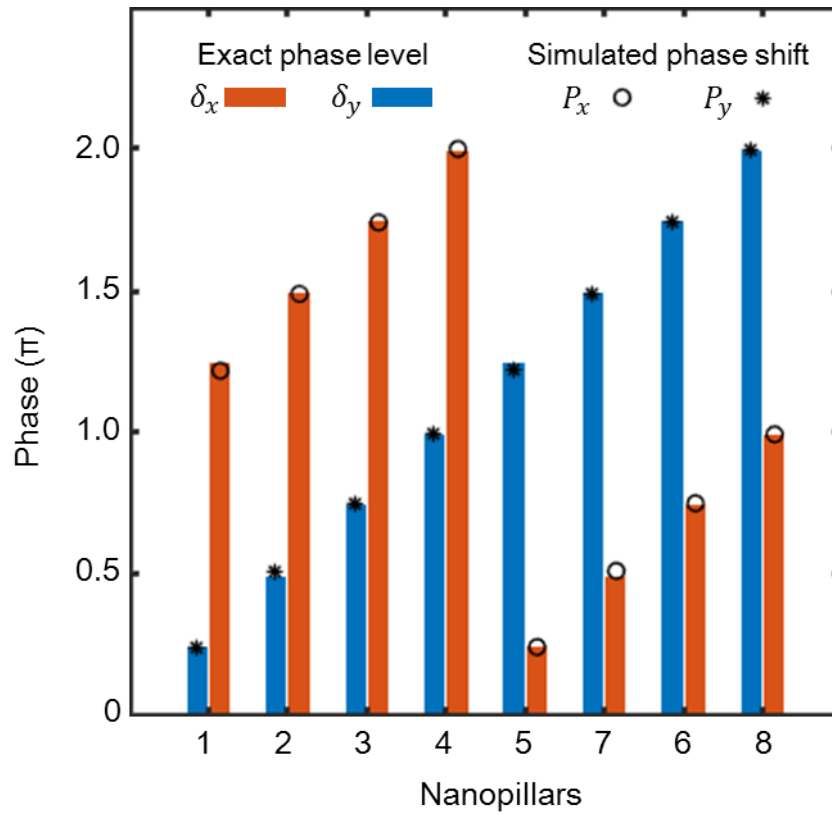
$$\langle U_N | U_N \rangle = \left| \cos\left(\frac{\alpha}{2}\right) e^{i\beta/2} E_{l_m}(r, \varphi) \begin{bmatrix} 1 \\ -i \end{bmatrix} + \sin\left(\frac{\alpha}{2}\right) e^{-i\beta/2} E_{l_n}(r, \varphi) \begin{bmatrix} 1 \\ i \end{bmatrix} \right|^2 \quad (\text{S25})$$

where $E_{l_m}(r, \varphi)$ and $E_{l_n}(r, \varphi)$ denote the magnitudes of the RCP and LCP POVs with topological charges l_m and l_n given by eq. S24. $\cos\left(\frac{\alpha}{2}\right)$ and $\sin\left(\frac{\alpha}{2}\right)$ determine the weights of RCP and LCP POV and β is the relative phase shift between them. The metasurface-generated PPB can be characterized by a linear polarizer with orientation angle χ from the x axis. The intensity of the PPB after transmission through a linear polarizer is expressed as:

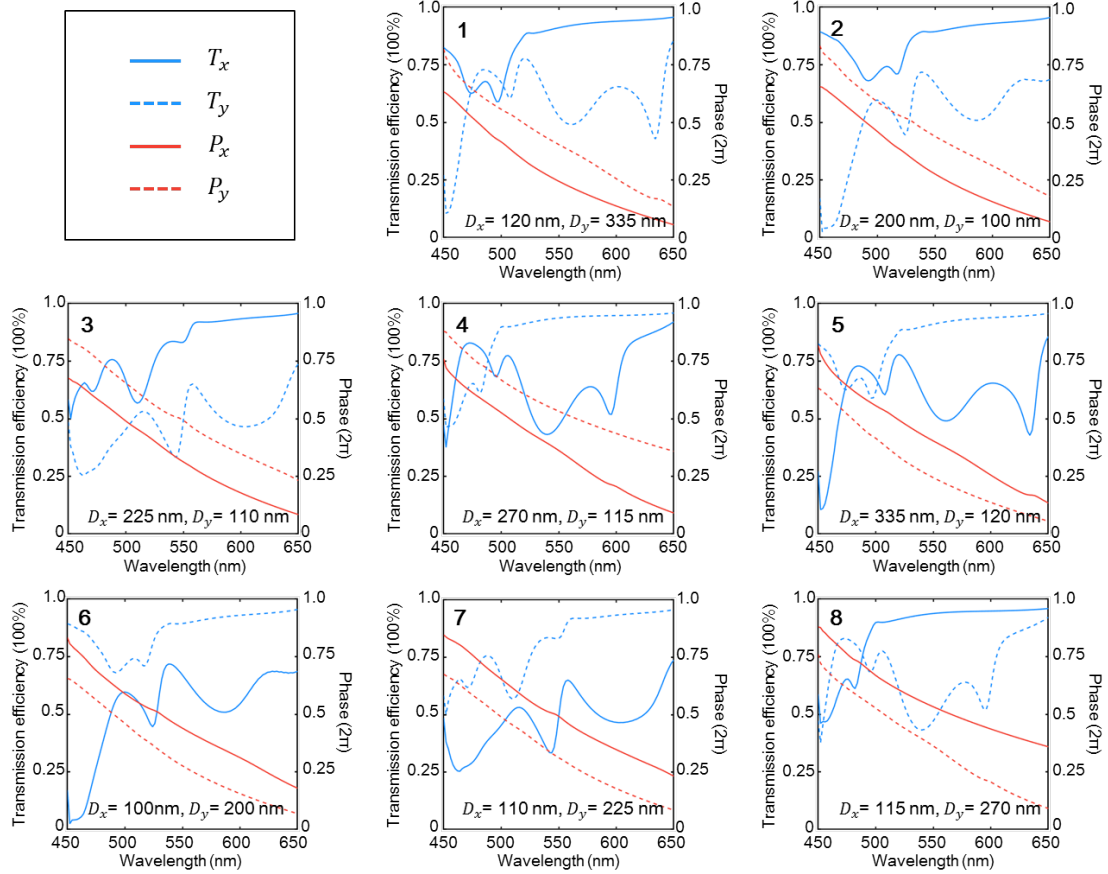
$$T_{LP} = \left| \begin{bmatrix} \cos^2 \chi & \cos \chi \sin \chi \\ \cos \chi \sin \chi & \sin^2 \chi \end{bmatrix} \cdot |U_N\rangle \right|^2 \quad (\text{S26})$$



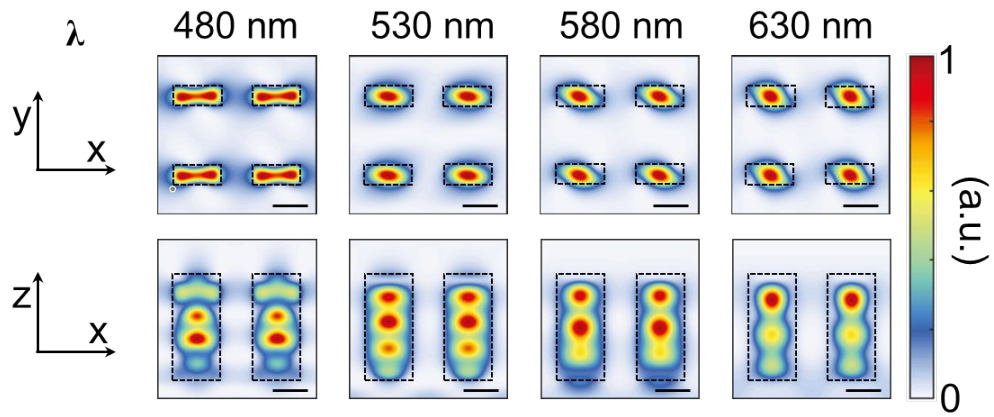
Supplementary Fig. S1. Simulated phase shifts (**a.** P_x ; **b.** P_y) and power transmission coefficients (**c.** T_x ; **d.** T_y) for x - and y - polarized light as functions of the rectangular nanopillar diameters (D_x and D_y) at a free-space wavelength of 530 nm.



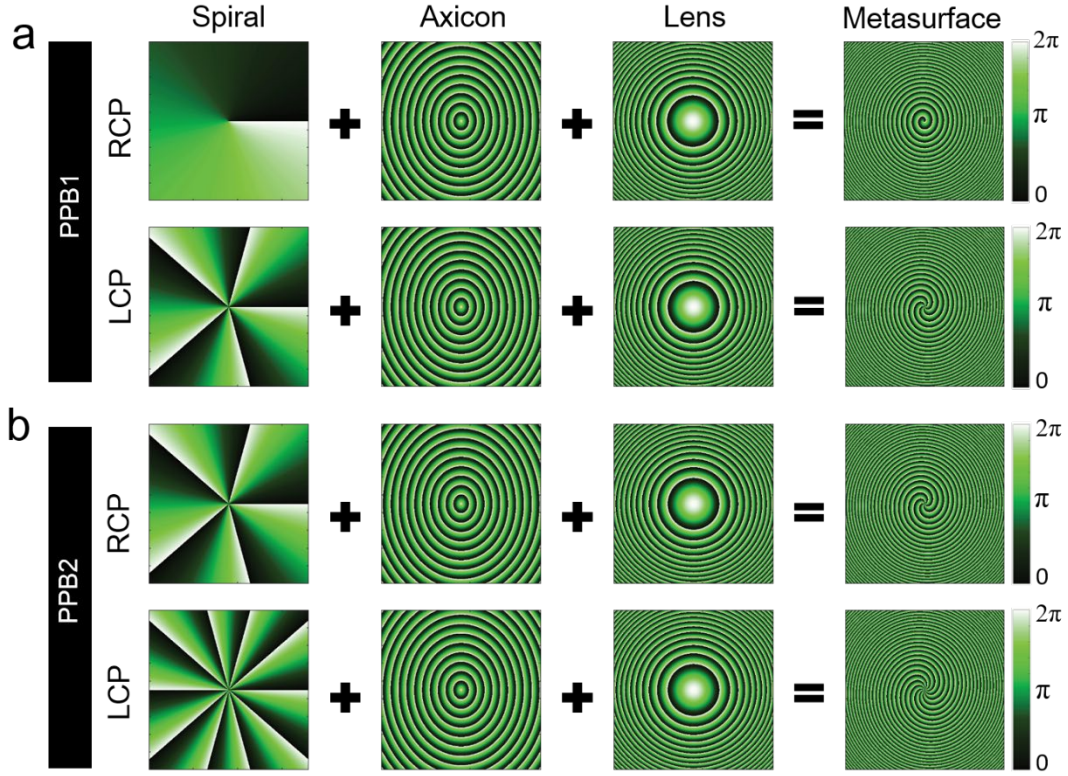
Supplementary Fig. S2. Eight level of discrete phase in the full range $[0, 2\pi]$ for δ_x and δ_y (depicted by red and blue bars, respectively) and simulated phase shifts P_x and P_y (depicted by circle and star symbols, respectively) of eight selected TiO₂ nanopillars at the designed wavelength of 530 nm. Each phase level corresponds to a specific TiO₂ nanopillar which is also a half-wave plate.



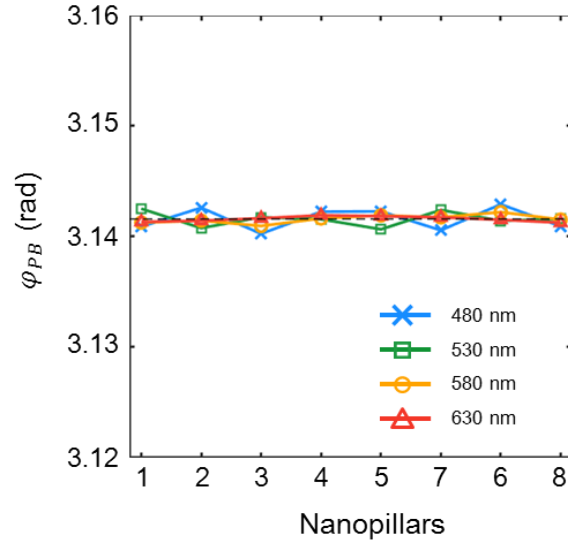
Supplementary Fig. S3. Wavelength dependence of power transmission efficiency (T_x and T_y) and phase shifts (P_x and P_y) of eight selected nanopillars (numbered 1-8) for x- and y-polarized light in the visible.



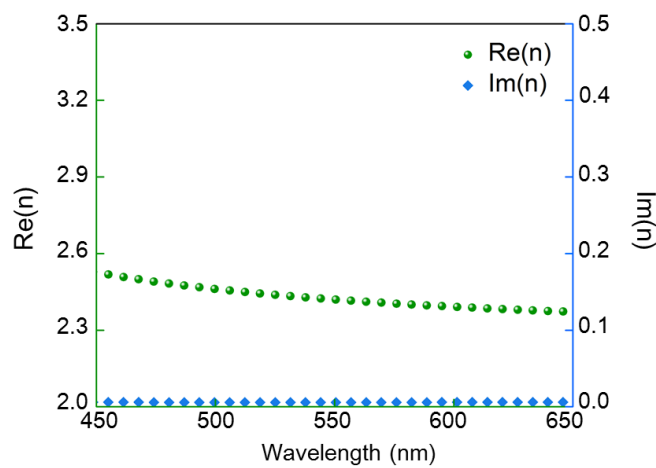
Supplementary Fig. S4. Simulated normalized magnetic energy density of the nanopillar array for various incident wavelengths. The dimensions of each nanopillar are $D_x = 270$ nm and $D_y = 115$ nm. Dashed black lines depict the boundaries of the nanopillars (top: x - y cross-section; bottom: x - z cross-section). Scale bar: 200 nm.



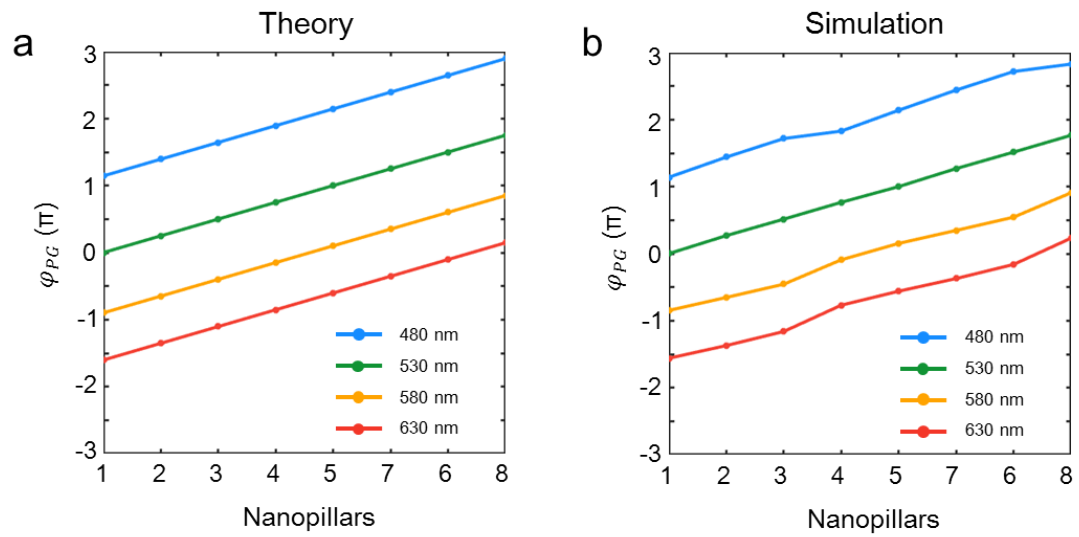
Supplementary Fig. S5. Phase distributions encoded on the metasurface for the generation of PPBs. **a** The metasurface MF1 for the generation of PPB1 should impart the phase profile $\varphi_1(x,y)$ with $l_m = 1$ for RCP light and another phase profile $\varphi_2(x,y)$ with $l_m = 5$ for LCP light. **b** The metasurface MF2 for the generation of PPB2 should impart the phase profile $\varphi_1(x,y)$ with $l_m = 5$ for RCP light and another phase profile $\varphi_2(x,y)$ with $l_m = 10$ for LCP light. The phase profiles $\varphi_1(x,y)$ and $\varphi_2(x,y)$ for MF1 and MF2 are the superposition of phase distributions of the spiral phase plate, axicon and lens and share the same values of $NA = 0.1$, $\gamma = 1.2$ and $f = 200 \mu\text{m}$.



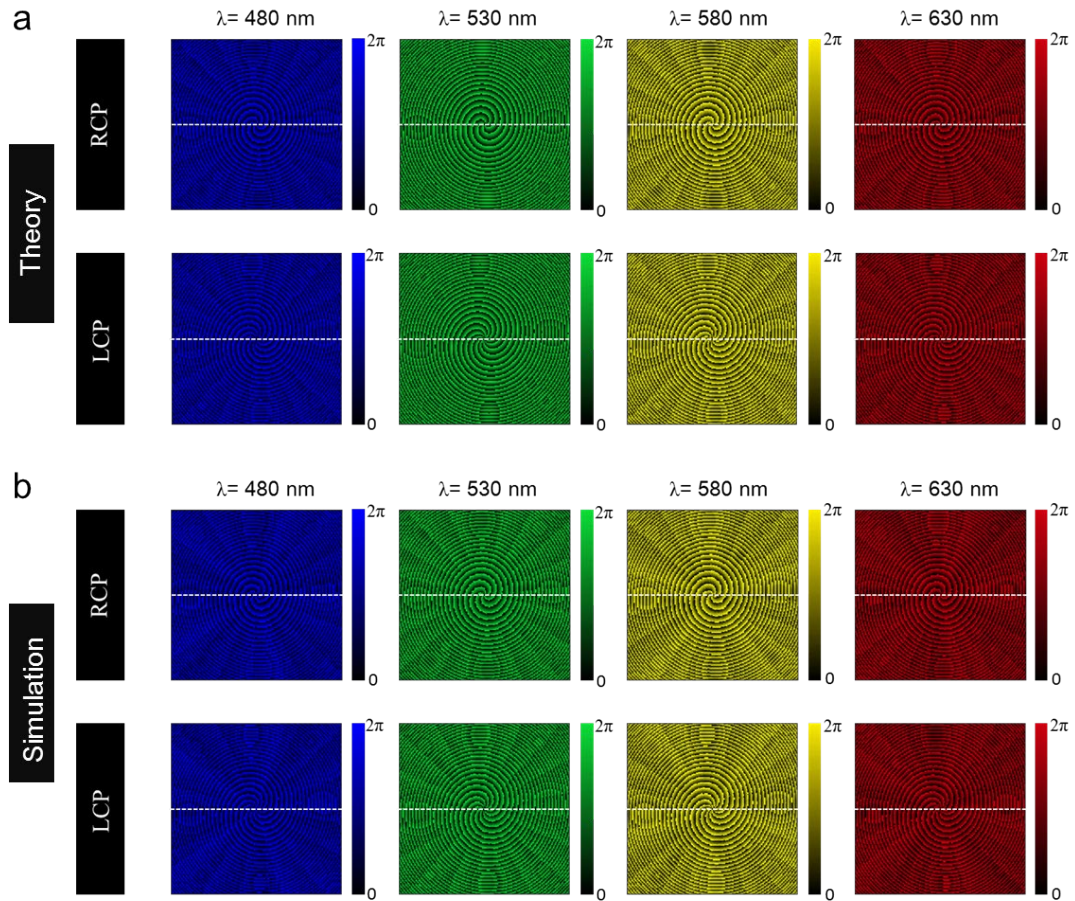
Supplementary Fig. S6. Theoretical and simulated geometric phases of eight selected nanopillars with same orientation angle of $\pi/2$. The black dashed line denotes the same theoretical geometric phase values of π at wavelengths of 480 nm, 530 nm, 580 nm and 630 nm. The cross, square, circle and triangle denote the simulated geometric phases at different incident wavelengths of 480 nm (blue), 530 nm (green), 580 nm (yellow) and 630 nm (red), respectively.



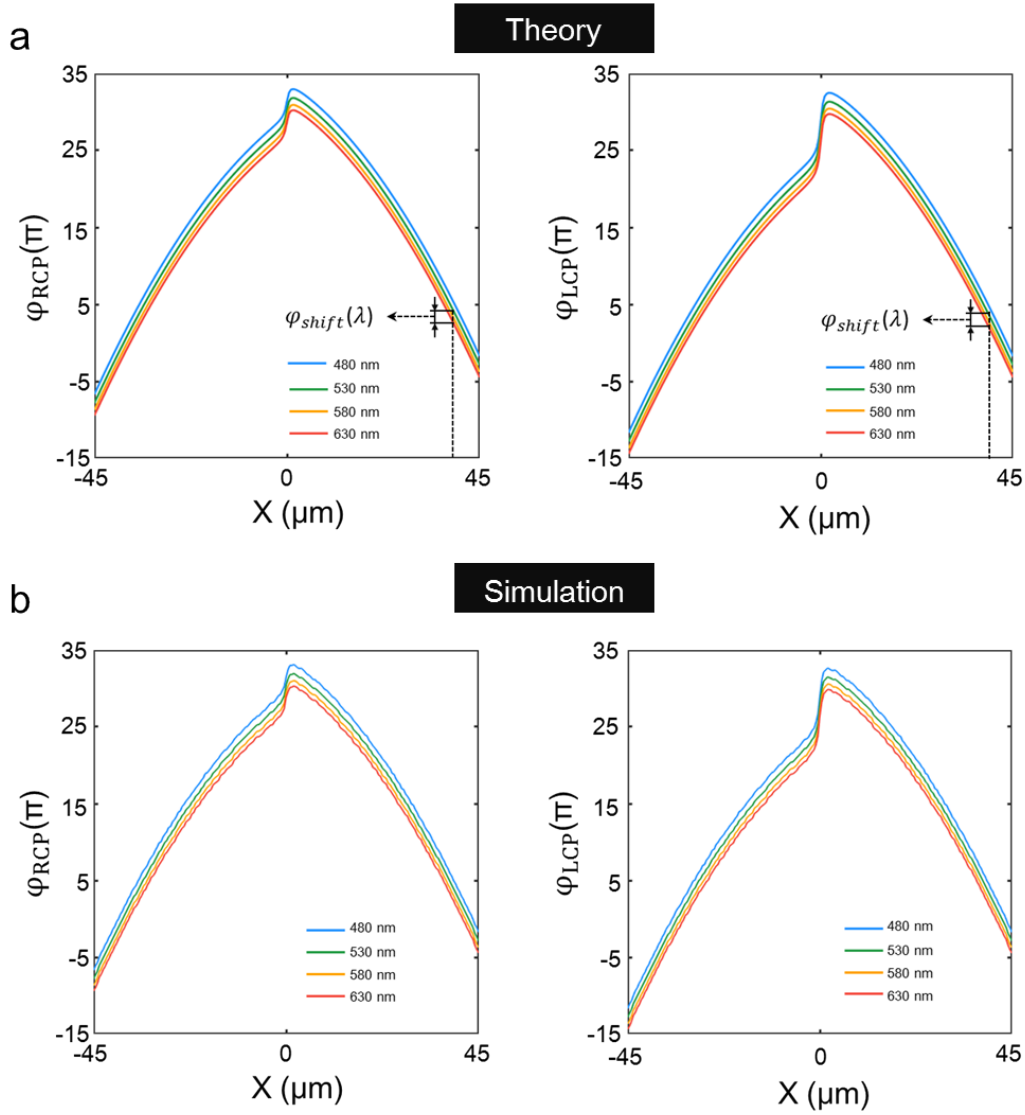
Supplementary Fig. S7. Complex refractive index of atomic layer deposition (ALD) amorphous titanium dioxide (TiO_2). The real (green circles) and imaginary (blue squares) part of the complex refractive index as a function of wavelength are measured by spectroscopic ellipsometry.



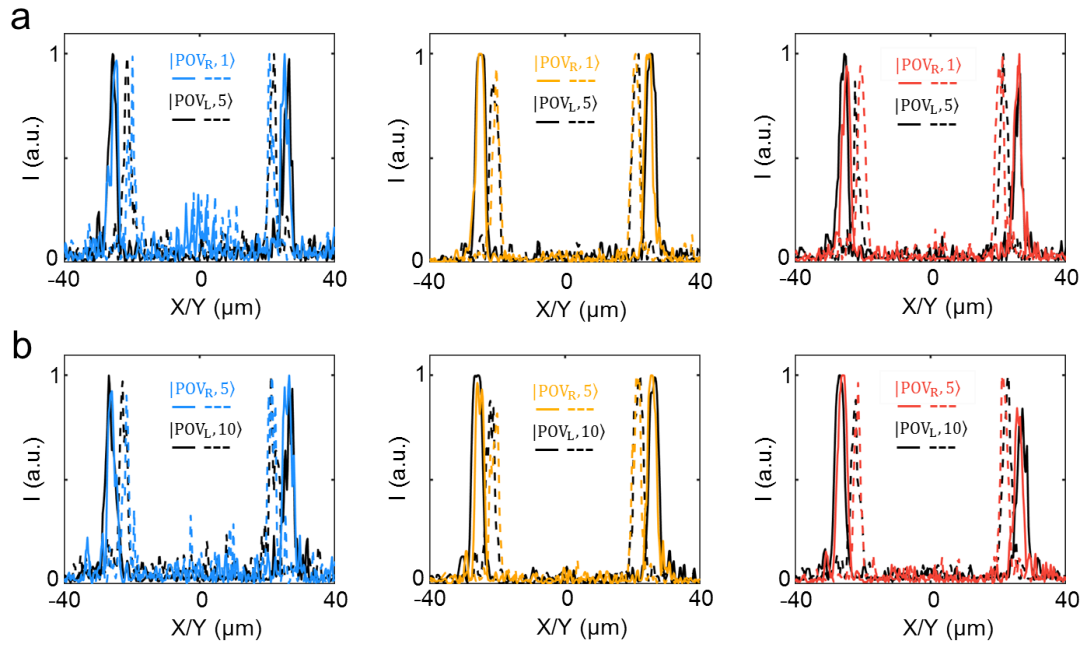
Supplementary Fig. S8. Theoretical (a) and simulated (b) propagation phases generated by 8-step nanopillars at different incident wavelength of 480 nm (blue), 530 nm (green), 580 nm (yellow) and 630 nm (red) can cover the entire 0 to 2π phase range.



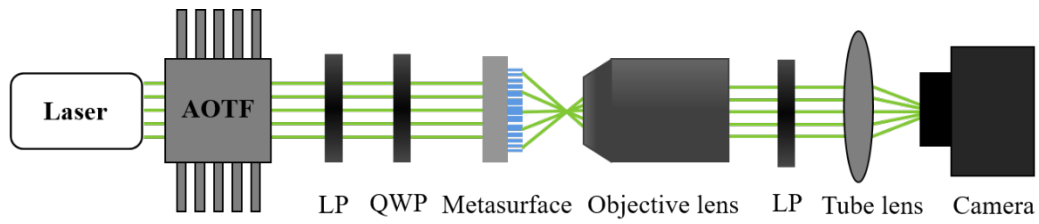
Supplementary Fig. S9. Theoretical and simulated in-plane phase profiles for RCP and LCP light offered by a broadband metasurface for generation of two orthogonal circularly polarized perfect vortices at different incident wavelength of 480 nm (blue), 530 nm (green), 580 nm (yellow) and 630 nm (red).



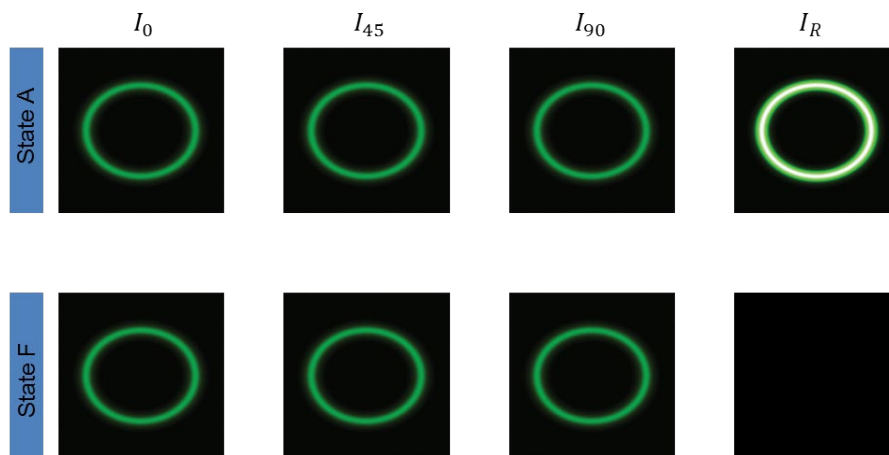
Supplementary Fig. S10. Cross sections of theoretical (a) and simulated (b) metasurface-imparted in-plane phase profiles along x -axis for RCP and LCP light at the incident wavelengths of 480 nm, 530 nm, 580 nm and 630 nm. $\varphi_{\text{shift}}(\lambda)$ is a wavelength-dependent and coordinate-independent constant phase shift and in accord with the $\varphi_{\text{constant}}(\lambda)$.



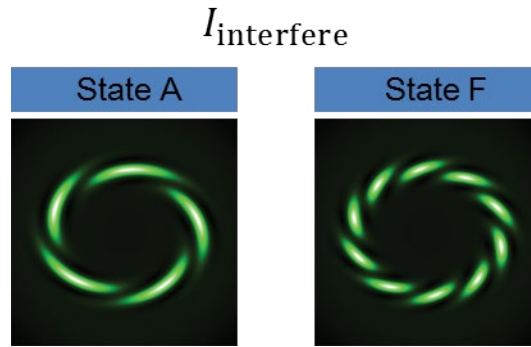
Supplementary Fig. S11. Normalized cross-sections of the annular intensity profiles of the optical vortices along x - and y - directions at wavelengths: 480 nm (blue), 580 nm (yellow) and 630 nm (red) at propagation distance of $z = 230 \mu\text{m}$, $195 \mu\text{m}$ and $180 \mu\text{m}$, respectively for MF1 (a) and MF2 (b).



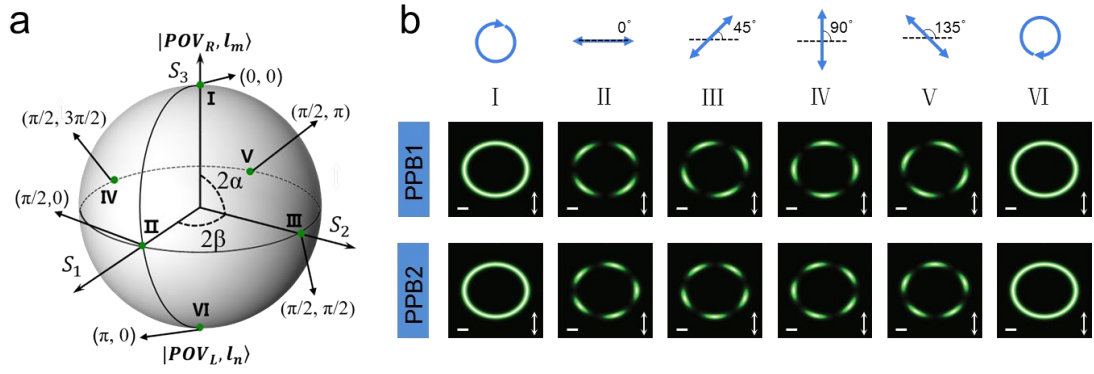
Supplementary Fig. S12. Experimental setup for measuring metasurface devices generating arbitrary states of PPBs on the HyOPS. A supercontinuum laser filtered by an acousto-optic tunable filter (AOTF) system passing through a linear polarizer (LP) and quarter waveplate (QWP) are converted into the desired polarization lights and incident on the metasurfaces. The transmitted lights are captured after filtering through a linear polarizer (LP).



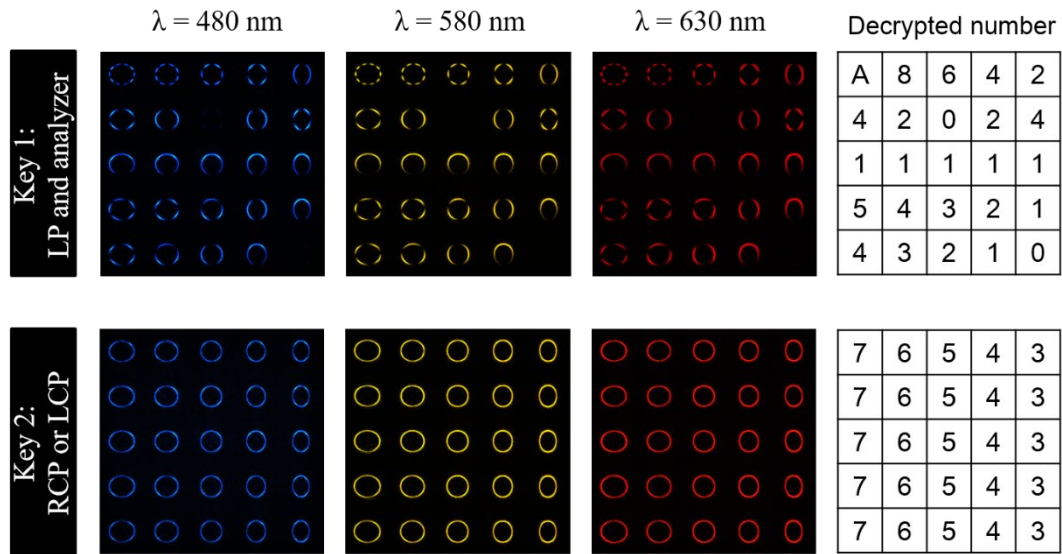
Supplementary Fig. S13. Calculated intensities of I_0 , I_{45} , I_{90} and I_R for state A and state F of the PPB in Fig. 1a performed by Stokes polarimetry.



Supplementary Fig. S14. Simulated interference patterns of state A and state F of the PPB in Fig. 1a. The two beam of state A and state F are with topological charges of $l_m = 5$ and $l_n = 10$, respectively.



Supplementary Fig. S15. Calculated intensities of the PPBs corresponding to the points on the HyOPS. **a** The six selected points on HyOPS represent the six states of PPB. **b** Top: the polarization states of the incident light. Bottom: the calculated annular intensity patterns corresponding to the points in **a** for PPB1 and PPB2 after transmission through a vertical linear polarizer depicted by the white double arrow. Scale bar: 10 μm .



Supplementary Fig. S16. Measured images with two customized keys at the wavelengths of 480 nm (blue), 580 nm (yellow) and 630 nm (red) at a propagation distance of $z = 230 \mu\text{m}$, 195 μm and 180 μm , respectively. According to the code chart, the first and second digits of two-digit hexadecimal numbers can also be decrypted.

Supplementary Table 1. The geometrical parameters of the eight nanopillars selected to cover the entire 2π phase range.

Number	Dx (nm)	Dy (nm)
1	120	335
2	200	100
3	225	110
4	270	115
5	335	120
6	100	200
7	110	225
8	115	270

Supplementary Table 2. The conversion efficiencies of the fabricated metasurfaces for generation of POVs. The errors are one standard deviation for repeated measurements (five in total).

Metasurface	480 nm	530 nm	580 nm	630 nm
MF 1 $ \text{POV}_R, l_1\rangle$	$35\% \pm 2\%$	$50\% \pm 2\%$	$42\% \pm 3\%$	$39\% \pm 2\%$
MF 1 $ \text{POV}_L, l_5\rangle$	$33\% \pm 2\%$	$54\% \pm 4\%$	$45\% \pm 3\%$	$40\% \pm 3\%$
MF 2 $ \text{POV}_R, l_5\rangle$	$31\% \pm 1\%$	$53\% \pm 2\%$	$42\% \pm 3\%$	$39\% \pm 2\%$
MF 2 $ \text{POV}_L, l_{10}\rangle$	$34\% \pm 3\%$	$51\% \pm 4\%$	$39\% \pm 2\%$	$42\% \pm 3\%$

Supplementary Table 3. Code chart of 256 hexadecimal numbers from 00 to FF represented by 256 different kinds of PPBs. Here, s_0 to s_{15} denote the sizes of PPBs depending on the γ ranging from 0.5 to 2.0 and p_0 to p_{15} denote the lobe numbers of PPBs depending on the $|p|$ ranging from 0 to 7.5.

	p_0	p_1	p_2	p_3	p_4	p_5	p_6	p_7	p_8	p_9	p_{10}	p_{11}	p_{12}	p_{13}	p_{14}	p_{15}
s_0	00	01	02	03	04	05	06	07	08	09	0A	0B	0C	0D	0E	0F
s_1	10	11	12	13	14	15	16	17	18	19	1A	1B	1C	1D	1E	1F
s_2	20	21	22	23	24	25	26	27	28	29	2A	2B	2C	2D	2E	2F
s_3	30	31	32	33	34	35	36	37	38	39	3A	3B	3C	3D	3E	3F
s_4	40	41	42	43	44	45	46	47	48	49	4A	4B	4C	4D	4E	4F
s_5	50	51	52	53	54	55	56	57	58	59	5A	5B	5C	5D	5E	5F
s_6	60	61	62	63	64	65	66	67	68	69	6A	6B	6C	6D	6E	6F
s_7	70	71	72	73	74	75	76	77	78	79	7A	7B	7C	7D	7E	7F
s_8	80	81	82	83	84	85	86	87	88	89	8A	8B	8C	8D	8E	8F
s_9	90	91	92	93	94	95	96	97	98	99	9A	9B	9C	9D	9E	9F
s_{10}	A0	A1	A2	A3	A4	A5	A6	A7	A8	A9	AA	AB	AC	AD	AE	AF
s_{11}	B0	B1	B2	B3	B4	B5	B6	B7	B8	B9	BA	BB	BC	BD	BE	BF
s_{12}	C0	C1	C2	C3	C4	C5	C6	C7	C8	C9	CA	CB	CC	CD	CE	CF
s_{13}	D0	D1	D2	D3	D4	D5	D6	D7	D8	D9	DA	DB	DC	DD	DE	DF
s_{14}	E0	E1	E2	E3	E4	E5	E6	E7	E8	E9	EA	EB	EC	ED	EE	EF
s_{15}	F0	F1	F2	F3	F4	F5	F6	F7	F8	F9	FA	FB	FC	FD	FE	FF

Supplementary Table 4. A portion of American Standard Code for Information Interchange.

HEX denote the hexadecimal numbers and ABBR/CHAR denote the abbreviation of control character or displayable character.

HEX	ABBR/ CHAR										
20	(Space)	30	0	40	@	50	P	60	`	70	p
21	!	31	1	41	A	51	Q	61	a	71	q
22	"	32	2	42	B	52	R	62	b	72	r
23	#	33	3	43	C	53	S	63	c	73	s
24	\$	34	4	44	D	54	T	64	d	74	t
25	%	35	5	45	E	55	U	65	e	75	u
26	&	36	6	46	F	56	V	66	f	76	v
27	'	37	7	47	G	57	W	67	g	77	w
28	(38	8	48	H	58	X	68	h	78	x
29)	39	9	49	I	59	Y	69	i	79	y
2A	*	3A	:	4A	J	5A	Z	6A	j	7A	z
2B	+	3B	;	4B	K	5B	[6B	k	7B	{
2C	,	3C	<	4C	L	5C	\	6C	l	7C	
2D	-	3D	=	4D	M	5D]	6D	m	7D	}
2E	.	3E	>	4E	N	5E	^	6E	n	7E	~
2F	/	3F	?	4F	O	5F	_	6F	o	7F	DEL

Reference

- [1] Ostrovsky, A., Rickenstorff-Parrao, C., Arrizón, V. Generation of the “perfect” optical vortex using a liquid-crystal spatial light modulator. *Opt. Lett.* 38, 534 (2013).
- [2] Gori, F., Guattari, G., Padovani, C. Bessel-Gauss beam. *Opt. Commun.* 64, 491(1987).
- [3] Goodman, J. *Introduction to Fourier Optics* (Roberts & Company, 2004).
- [4] Mongia, R. K., Ittipiboon, A. Theoretical and experimental investigations on rectangular dielectric resonator antennas. *IEEE Trans. Antenn. Propag.* 45, 1348–1356 (1997).
- [5] Li, Z., Chen, C., Guan, Z., Tao, J., Chang, S., Dai, Q., Xiao, Y., Cui, Y., Wang, Y., Yu, S., Zheng, G., Zhang, S. Three-Channel Metasurfaces for simultaneous meta-holography and meta-nanoprinting: a single-cell design approach. *Laser Photonics Rev.* 14(6), 2000032 (2020).
- [6] Huo, P., Zhang, C., Zhu, W., Liu, M., Zhang, S., Zhang, S., Chen, L., Lezec, H., Agrawal, A., Lu, Y. and Xu, T. Photonic spin-multiplexing metasurface for switchable spiral phase contrast imaging. *Nano. Lett.* 20, 2791-2798 (2020).
- [7] Fan, Z. B., Shao, Z. K., Xie, M. Y., Pang, X. N., Ruan, W. S., Zhao, F. L., Chen, Y., Yu, S., Dong, J. W. Silicon nitride metalenses for close-to-one numerical aperture and wide-angle visible imaging. *Phys. Rev. Appl.* 10(1), 014005 (2018).
- [8] Chen, W. T., Khorasaninejad, M., Zhu, A. Y., Oh, J., Devlin, R. C., Zaidi, A., Capasso, F. Generation of wavelength-independent subwavelength Bessel beams using metasurfaces. *Light Sci. Appl.* 6(5), e16259-e16259 (2017).
- [9] Schaefer, B., Collett, E., Smyth, R., Barrett, D., Fraher, B. Measuring the Stokes polarization parameters. *Am. J. of Phys.* 75(2), 163-168 (2007).